The Astrophysical Journal, 950:38 (25pp), 2023 June 10 https://doi.org/10.3847/1538-4357/acc8cd

Unraveling Twisty Linear Polarization Morphologies in Black Hole Images

Razieh Emami[1], Angelo Ricarte[1,2], George N. Wong[3,4], Daniel Palumbo[1,2], Dominic Chang[2], Sheperd S. Doeleman[1,2], Avery E. Broderick[5,6], Ramesh Narayan[1,2], Maciek Wielgus[7], Lindy Blackburn[1,2], Ben S. Prather[8], Andrew A. Chael[9,18], Richard Anantua[1,2,10], Koushik Chatterjee[2], Ivan Marti-Vidal[11,12], Jose L. Gómez[13], Kazunori Akiyama[14,15,16], Matthew Liska[1], Lars Hernquist[1], Grant Tremblay[1], Mark Vogelsberger[17], Charles Alcock[1], Randall Smith[1], James Steiner[1], Paul Tiede[1,2], and Freek Roelofs[1,2]

[1] Center for Astrophysics | Harvard & Smithsonian, 60 Garden Street, Cambridge, MA 02138, USA; razieh.emami_meibody@cfa.harvard.edu
[2] Black Hole Initiative at Harvard University, 20 Garden Street, Cambridge, MA 02138, USA
[3] School of Natural Sciences, Institute for Advanced Study, 1 Einstein Drive, Princeton, NJ 08540, USA
[4] Princeton Gravity Initiative, Princeton University, Princeton, NJ 08544, USA
[5] Perimeter Institute for Theoretical Physics, 31 Caroline Street North, Waterloo, ON, N2L 2Y5, Canada
[6] Department of Physics and Astronomy, University of Waterloo, 200 University Avenue West, Waterloo, ON, N2L 3G1, Canada
[7] Max-Planck-Institut für Radioastronomie, Auf dem Hügel 69, D-53121 Bonn, Germany
[8] Department of Physics, University of Illinois, 1110 West Green Street, Urbana, IL 61801, USA
[9] Princeton Gravity Initiative, Jadwin Hall, Princeton University, Princeton, NJ 08544, USA
[10] Department of Physics & Astronomy, The University of Texas at San Antonio, One UTSA Circle, San Antonio, TX 78249, USA
[11] Departament d'Astronomia i Astrofísica, Universitat de València, C/Dr. Moliner 50, E-46100 Burjassot Spain
[12] Observatori Astronòmic, Universitat de València, C/Catedràtico Beltrán 2, E-46980 Paterna, Spain
[13] Instituto de Astrofísica de Andalucía-CSIC, Glorieta de la Astronomía s/n, Spain
[14] Massachusetts Institute of Technology Haystack Observatory, 99 Millstone Road, Westford, MA 01886, USA
[15] Mizusawa VLBI Observatory, National Astronomical Observatory of Japan, 2-12 Hoshigaoka, Mizusawa, Oshu, Iwate 023-0861, Japan
[16] Black Hole Initiative, Harvard University, 20 Garden Street, Cambridge, MA 02138, USA
[17] Department of Physics, Kavli Institute for Astrophysics and Space Research, Massachusetts Institute of Technology, Cambridge, MA 02139, USA
Received 2022 October 9; revised 2023 March 11; accepted 2023 March 28; published 2023 June 8

Abstract

We investigate general relativistic magnetohydrodynamic simulations to determine the physical origin of the twisty patterns of linear polarization seen in spatially resolved black hole images and explain their morphological dependence on black hole spin. By characterizing the observed emission with a simple analytic ring model, we find that the twisty morphology is determined by the magnetic field structure in the emitting region. Moreover, the dependence of this twisty pattern on spin can be attributed to changes in the magnetic field geometry that occur due to the frame dragging. By studying an analytic ring model, we find that the roles of Doppler boosting and lensing are subdominant. Faraday rotation may cause a systematic shift in the linear polarization pattern, but we find that its impact is subdominant for models with strong magnetic fields and modest ion-to-electron temperature ratios. Models with weaker magnetic fields are much more strongly affected by Faraday rotation and have more complicated emission geometries than can be captured by a ring model. However, these models are currently disfavoured by the recent EHT observations of M87*. Our results suggest that linear polarization maps can provide a probe of the underlying magnetic field structure around a black hole, which may then be usable to indirectly infer black hole spins. The generality of these results should be tested with alternative codes, initial conditions, and plasma physics prescriptions.

Unified Astronomy Thesaurus concepts: Black hole physics (159); Event horizons (479); Plasma astrophysics (1261); Magnetohydrodynamical simulations (1966)

1. Introduction

The Event Horizon Telescope Collaboration (EHTC) has recently published the first polarized image of the supermassive black hole (SMBH) at the center of giant elliptical galaxy Messier 87 (hereafter M87*; Event Horizon Telescope Collaboration et al. 2019a, 2019b, 2019c, 2019d, 2019e, 2019f, 2021a, 2021b). These results feature resolved linear polarization with a diffraction-limited resolution corresponding to approximately $5\,GM/c^2$, where M is the mass of the SMBH, G is the gravitational constant, and c is the speed of light. The image reveals an asymmetric ring-like structure with a bright region at its southern edge, attributed to the Doppler effect and the bending of light originating from the synchrotron emission of orbiting relativistic electrons in the vicinity of the event horizon.

The polarimetric image of M87* BH presented in Event Horizon Telescope Collaboration et al. (2021a, 2021b) provides information on both the degree and the directionality of linear polarization where the latter is determined by the electric vector position angle (hereafter EVPA). Quantifying the twistiness of the polarized images, defined as the smooth azimuthal change of the EVPA within the ring pattern, offers us new insights into the structure of magnetic field, putting strong constraints on the nature of the ring and the emission region.

The observed image of M87* from EHTC reveals an azimuthally spiraling pattern of the EVPA. Motivated by this, Palumbo et al. (2020) used a particular decomposition of linear polarization to azimuthal modes identified with complex

[18] NASA Hubble Fellowship Program, Einstein Fellow.

coefficients β_m. They found that the rotationally symmetric mode of a Fourier decomposition of a linear polarization pattern can distinguish between theoretical models. It was shown in Event Horizon Telescope Collaboration et al. (2021b) and Palumbo et al. (2020) that $m = 2$ (i.e., β_2) is the dominant contribution in the characterization of the magnetized accretion model. Furthermore, the β_2 phase matches very well with the theoretically expected behavior of the polarized map (see Event Horizon Telescope Collaboration et al. 2021b, for more details). Finally, both the amplitude and the phase of β_2 are sensitive to the magnetic field geometry and the black hole spin. However, a detailed characterization of their correlation to the plasma astrophysics and the spacetime geometry remains elusive.

Narayan et al. (2021) modeled the polarimetric image of a BH using a simple toy model comprising a magnetized ring of emission located near the Schwarzschild event horizon. The model comprises an equatorial emission and fluid velocity with an arbitrary emission radius, magnetic field structure, and observer's inclination. Gelles et al. (2021) further extended this toy model to include the effect of BH spin by moving from the Schwarzschild spacetime to the Kerr geometry. The simplicity of the aforementioned toy models make them remarkably useful to do extensive exploration of different emission models and magnetic field structure. Such an investigation is computationally very expensive using the general relativistic magnetohydrodynamical simulations (GRMHD). Yet, the validity of the assumptions made in such toy models remains elusive. Furthermore, it is not very clear what drives the β_2 in the simple ring model.

Positron effects on polarized emission, including EVPA patterns, have been found to be dependent on plasma thermodynamics in Anantua et al. (2020) and Emami et al. (2021). The linearly polarized portion of ray-traced images therein are supported on bilaterally asymmetric jet regions along with emitting rings around the Kerr magnetosphere. The global EVPA structure ranges from radial to spiral based on thermodynamic parameters and their interaction with the positron fraction of the plasma.

In this work, we perform a comprehensive study of the driving sources of β_2 in simulated models of M87*. We utilize the same GRMHD simulations used in Event Horizon Telescope Collaboration et al. (2019e, 2021b) generated with the PATOKA pipeline (Wong et al. 2022), with a variety of different accretion states, BH spins, and emission physics. To model the polarized images of M87*, we make use of the general relativistic radiative transfer (GRRT) framework implemented in code IPOLE (Mościbrodzka & Gammie 2018). We find the emission radius and link the magnetic field structure and velocity field at the emission location to the pattern of the EVPA. We investigate many effects which might contribute to the signal, including the spatial origin of the emission, Faraday rotation, and relativistic effects. We find out that the signal strongly depends on the magnetic field geometry along with the BH spin. Our analysis shows that, while the ring model works reasonably well for the case of a magnetically arrested disk (MAD; Bisnovatyi-Kogan & Ruzmaikin 1974; Igumenshchev et al. 2003; Narayan et al. 2003), it has some limitations trying to fully capture the case of the standard and normal evolution (SANE; De Villiers et al. 2003; Gammie et al. 2003; Narayan et al. 2012). Furthermore, the overall consistency is reduced when we consider cooler electrons. We conclude that the phase of the β_2 indirectly probes the magnetic field geometry. Consequently, trends in β_2 are fundamentally linked to different magnetic field structures.

The paper is organized as follows. Section 2 describes our methodology, including the GRMHD simulation 2.1, the actual ray tracing 2.2, magnetic field polarimetry 2.3, the geometrical ring model 2.4, and azimuthally expanded polarized mode (β_2) 2.5. Section 3 focuses on the polarimetric analysis, including the time-averaged polarized images 3.1, calculation of the optical and the Faraday depths 3.2, the locus of emission 3.3, the correlation between the phase of the β_2 and the BH spin 3.4, drivers of the β_2 3.5, the impact of the magnetic field on the phase of the β_2 3.5.3, and the influence of Faraday rotation 3.6. The conclusion is provided in Section 4.

2. Methodology

In this section, we describe how we produce the polarized images of M87*. More details about the simulation procedure and codes used can be found in Wong et al. (2022).

2.1. GRMHD Simulations

We use IHARM simulations by Gammie et al. (2003) and Prather et al. (2021) from the standard library of 3D time-dependent GRMHD simulations performed in Event Horizon Telescope Collaboration et al. (2019e, 2021b). These ideal GRMHD simulations are initialized with a weakly magnetized torus of plasma orbiting in the equatorial plane around a BH. Instabilities like the magneto-rotational instability (Balbus & Hawley 1991) drive the torus into a turbulent state, which enables angular momentum transport and inward accretion of the matter onto the central black hole. The system tends toward a state with a mildly magnetized midplane, a coronal component where the gas to magnetic pressure $\beta \equiv P_g/P_B \simeq 1$ with a very strongly magnetized funnel region near the BH poles. The details of the outcome also depends on the strength and the geometry of the initial magnetic field.

Due to the initial condition, the first part of each simulation is dominated by a transient state as a turbulent accretion develops. During this transient state, the accretion rate grows, and the infalling plasma heats up and begins to emit radiation. In order to ensure that this artificial initial transient state does not influence our results, we run each simulation until at least $t = 10^4\, GM/c^3$, by which point the accretion flow close to the BH, which produces vast majority of the signal at 230 GHz, reaches a steady state. GRMHD fluid snapshots are saved every 5 GM/c^2 over the duration of the simulation; the time range of the initial transient state is found by analyzing the fluid snapshot data so that the "steady-state" epoch of the simulation can be identified.

For GRMHD simulations with non-zero BH angular momentum, we study the cases where the BH angular momentum J is aligned (parallel or antiparallel) with the angular momentum of the accretion flow. Ideal GRMHD simulations are invariant under mass rescaling and thus our (anti-)aligned systems are effectively described by just two parameters: the BH angular momentum (spin) and the near horizon magnetic flux Φ_B. The dimensionless BH spin, hereafter $a \equiv Jc/GM^2$, is limited to $-1 \leqslant a \leqslant 1$. The dimensionless magnetic flux at the horizon is $\phi \equiv \Phi(\dot{M} r_g^2 c)^{-1/2}$ (where $r_g \equiv GM/c^2$ refers to the gravitational radius) determines if the accretion is in a SANE ($\phi \simeq 5$) or MAD ($\phi \gtrsim 50$) state.

The numerical methods used to solve the MHD equations often fail in the regions with low density ρ and strong magnetic fields B. These failures are dealt with through the application of floors, which inject artificial density or energy, producing unreliable plasma temperatures. To ensure that the artificial floors do not influence simulated observations, we employ a σ cutoff during the radiative transfer calculation and mask regions where $\sigma = B^2/\rho > 1$, following Event Horizon Telescope Collaboration et al. (2019e). Typically the impact on SANE simulations is negligible, as the flagged region is concentrated around the axis, where very little emission is predicted. In MAD models, the masked region may occur in different locations of the simulation, and it is expected to result in slightly dimmer millimeter wavelength images. While this problem is fundamental and important to study further, we expect that it should not appreciably impact the image morphology, and proceed under this assumption. In this work, we adopt $\sigma = 1$ as the boundary between the regions with reliable plasma parameters and the aforementioned flagged region. To illustrate the possible impact of the σ in our analysis, in Figures 3 and 4, we present the contour of $\sigma = 1$ with a dashed–dotted white line. Furthermore, in Figure 12, we present the color plot of the $\log_{10}\sigma$ in the source R versus Z plane for the time and azimuthally averaged GRMHD simulations of MAD and SANE simulations. The emission location is marked as the black star. It is generally seen that the the emission location is fairly consistent with the white region, associated with $\sigma = 1$ as adopted in this work.

2.2. Imaging

In order to generate polarized images of M87*, we use the GRRT code IPOLE (Mościbrodzka & Gammie 2018). Each image is produced with a 160 μas field of view (FOV) and a resolution of 320×320 pixels, with each image containing the four Stokes parameters, *I, Q, U*, and *V*. IPOLE first solves for the null geodesic equations from the camera through the source, then the polarized radiative transfer equations forward along with the geodesic. Polarized synchrotron emission, self-absorption, Faraday rotation, and Faraday conversion are also taken into account in making the polarized images. For each set of model parameters (see below), images are produced over the entire steady-state time range identified in the GRMHD simulations.

Unlike in the GRMHD simulations, the GRRT calculation, which relies on the emission, absorption, and rotation transfer coefficients, is not scale invariant. Thus, while performing the ray tracing, we must set two physical scales for the system. The first scale is the characteristic system length, which is computed as $L = GM/c^2$. The second scale is determined by the simulation mass-density parameter, which is set by the observed flux density at 230 GHz which is chosen to be $F_\nu \simeq 0.5$ Jy (Event Horizon Telescope Collaboration et al. 2019d). Following Event Horizon Telescope Collaboration et al. (2019e), we have also fixed the inclination of the source to be 17 deg for retrograde and 163 deg for the prograde spins.

Next, to set the plasma temperature, we choose a different strategy than the one usually adapted in GRMHD simulations. In particular, we replace the thermal equilibrium approximation with a collisionless plasma in which electrons and ions most likely reach two different temperatures (Shapiro et al. 1976; Narayan & Yi 1995). Hence, as in previous work (e.g., Event Horizon Telescope Collaboration et al. 2019e, 2021b), we modulate the ion-to-electron temperature ratio via the prescription of Moscibrodzka et al. (2016):

$$\frac{T_i}{T_e} = R_{\rm high}\frac{\beta^2}{1+\beta^2} + R_{\rm low}\frac{1}{1+\beta^2}. \quad (1)$$

Here, β is the ratio of gas to magnetic pressure, and $R_{\rm high}$ and $R_{\rm low}$ are free parameters, allowed to vary with guidance from simulations that include electron heating. In our "Fiducial" set of models, we set $R_{\rm low} = 1$ and $R_{\rm high} = 20$, values favored by recent simulations (Chael et al. 2018; Mizuno et al. 2021). In our "Faraday Thick" set of models, on the other hand, we set $R_{\rm low} = 10$ and $R_{\rm high} = 160$, considered large values for each parameter. The electrons are colder in the Faraday Thick models, requiring increased mass density to match the observed flux of M87*. Both the lower temperature and the increased density makes this model much thicker to Faraday rotation than the Fiducial case, which plays an important role in decreasing the linear polarization fraction and modifying the EVPAs of a given region. A significant variation of the Faraday depth toward M87* has been reported by Goddi et al. (2021), motivating us to address both regimes.

The version of IPOLE that we use has been modified to record the spatial distribution of the emission that contributes to an image. Notice that this value depends on the location of the observer, due to both absorption (which occurs as light travels along the geodesic) and the anistropy of synchrotron emission (which makes the relevant emission a function of the line of sight through any particular points in space). In practice, we compute the observed emission for each pixel in an image and then sum over the pixels. For the geodesic corresponding to any image pixel, it is trivial to compute the effects of absorption along the geodesic by evaluating the optical depth between each point along that pixel's geodesic and the camera at infinity. The local (angle-dependent) emissivity can be directly computed at each event along the geodesic and multiplied into the optical depth extinction to calculate the local contribution to the final observed flux density. After repeating this procedure for each image's pixel, a histogram of all local contributions to the final image can be computed. This histogram represents the origin of all observed emission. More detail can be found in Section 3.2.1 of Wong et al. (2022).

2.3. Magnetic Field Polarity

The equations of ideal GRMHD are invariant under a sign flip of the magnetic field direction. Previous EHTC studies have considered only the case where the overall magnetic field polarity is parallel to that of the disk angular momentum. As we shall show however, this choice impacts the linear polarization structure in the images because of the Faraday rotation that is in place when the linear polarization passes through a magnetized plasma. Consequently, in generating images, we consider two distinct cases: one set with the magnetic field vector aligned with the disk angular momentum and the other is anti-aligned. Below, we examine both of these cases, calling them $\rm FR_1$ and $\rm FR_2$, respectively.

2.4. Geometric Ring Model

To build intuition for the polarized images of the M87* accretion flow produced by the EHT (Event Horizon Telescope Collaboration et al. 2021b), Narayan et al. (2021) constructed a

toy model for the synchroton emission from a thin ring of magnetized fluid orbiting a Schwarzschild black hole. This model assumes an optically thin ring of fluid at a single Boyer–Lindquist radius with an axisymmetric magnetic field and fluid velocity. Predictions for the observed polarization pattern on the viewing screen take the shape of a lensed ring of polarization vectors.

Gelles et al. (2021) extended the ring model to address equatorial emission in a Kerr spacetime and also specified the emission from highly lensed sub-images for which geodesics complete one or more half-orbits around the black hole. The Gelles model found that, assuming all other fluid parameters are equivalent, the effect of spin on the direct image polarization is very weak; therefore, the difference in polarization patterns that trend with spin are being driven indirectly, likely through modification of the underlying velocity and magnetic field directions, as we will show.

As shown in the GRMHD comparison paper by Narayan et al. (2021), these toy models can be used to produce non-infinitesimal rings by evaluating them over a range of radii and applying an envelope function to the underlying emissivity. D. Palumbo et al. (2023, in preparation) applied this procedure to the Gelles et al. (2021) model in Kerr metric to produce the image generation and model-fitting code "Kerr Bayesian Accretion Modeling" (`KerrBAM`), which we use to generate toy model images throughout the paper. `KerrBAM` generates model image by semi-analytically ray tracing backward from the observer screen to an arbitrarily inclined equatorial plane in Boyer–Lindquist coordinate, producing grids of radii and azimuthal angles. Given an axisymmetric prescription for the fluid velocity and magnetic field penetrating the plane, in addition to an envelope function $\mathcal{J}$, the synchrotron emissivity can be predicted for a given spectral index, which we take it to be 1 at 230 GHz (see the discussion in Section 2.2 of Narayan et al. (2021)). Throughout this paper, we use an axisymmetric ring profile given by:

$$\mathcal{J}_{\rm ring}(r) = \exp\left(-4\ln 2\frac{(r-R)^2}{w^2}\right), \tag{2}$$

where R is the peak radius and w is the full width of half maximum of the intensity profile. Note that the true emissivity also depends on the details of lensing, Doppler boosting, and the angle between geodesics and the local magnetic field, all of which are accounted for in `KerrBAM` for arbitrary photon winding numbers. However, the model does not contain any Faraday effects and thus does not meaningfully predict fractional polarization. Consequently, the ring model is most useful in the context of our paper as a predictor of the resolved structure of the EVPA.

2.5. Polarization Spirals and β_2

Palumbo et al. (2020) found that the magnetization state in simulations of the M87* accretion flow was strongly encoded in the spiraling structure of the EVPA, with more radially directed EVPA corresponding the SANE models and more spiraling or circular EVPA patterns corresponding to MADs. To differentiate between the MAD and SANE models more quantitatively, they proposed an azimuthal decomposition of the polarized image to isolate symmetric patterns in the EVPA with respect to the image azimuthal angle φ, when averaged over image radius ρ:

$$\beta_m = \frac{1}{I_{\rm tot}}\int_0^{\infty}\int_0^{2\pi} P(\rho,\,\varphi)\, e^{-im\varphi}\,\rho {\rm d}\varphi\,{\rm d}\rho, \tag{3}$$

$$I_{\rm tot} = \int_0^{\infty}\int_0^{2\pi} I(\rho,\,\varphi)\,\rho {\rm d}\varphi\,{\rm d}\rho. \tag{4}$$

where I refers to the the intensity while $P = Q + iU$ describes the linear polarization with Q and U referring to the Stokes parameters. Here, each coefficient β_m, which is normalized by the total image flux, is a complex coefficient with a phase that encodes the orientation of the spiral and an amplitude that is proportional to the average linear fractional polarization. Crucially, the $m = 2$ mode is rotationally symmetric; intuitively, a nearly axisymmetric flow viewed at nearly face-on inclination (as is the case for M87*) would produce a nearly rotationally symmetric image on the observer screen. Palumbo et al. (2020) found that, as expected, the β_2 mode is indeed the most informative coefficient for discriminating the accretion states, as the phase directly relates to the underlying magnetic field orientation in the limit of weak Faraday effects. Furthermore, Event Horizon Telescope Collaboration et al. (2021b) found that the phase of β_2 was more constraining than any other polarized image metric when comparing images from EHT data to GRMHD simulations. Of interest in this work is how strongly the β_2 phase can be related to the magnetic field in GRMHD simulations in two regimes of Faraday effect strength, as well as investigating the cause of the strong dependence on spin in the β_2 phase identified in Palumbo et al. (2020).

As in Event Horizon Telescope Collaboration et al. (2021b), we use the default image centering of the GRMHD library (which corresponds to a zero angular momentum photon at the screen center) when evaluating β_2, rather than recentering based on an empirical ring search. As evaluated in the discussion of Palumbo et al. (2020), the amplitude of β_2 decays quadratically in the centering error (as a fraction of the ring diameter), while phase effects enter only at higher order. In highly asymmetric images, the selection of an appropriate image center in observations may be more complicated, involving image-domain feature extraction; one might also choose the image center that maximizes the β_2 amplitude.

2.6. From GRMHD Simulation to the Geometrical Ring Model

Having introduced the GRMHD models and the geometrical ring model, here we briefly discuss how to make the connection between the two. This is essential because the ring model chooses an arbitrary value for the magnetic and the velocity fields. Consequently, to make a direct link between the β_2 phase from the GRMHD and the ring model, we shall make use of the *B/V* fields from the GRMHD simulations, which requires some coordinate transformations. More appropriately, while the GRMHD snapshots are given in the Kerr–Schild coordinate, the Ring model is based on the Boyer–Lindquist coordinate.

Comparison between GRMHD and the ring model requires establishing a suitable mapping that relates a given simulation to a ring model product. We created this mapping for each simulation by first selecting the radius of emission in the ring model to be the same as the peak emission radius of the chosen simulation, (see Figure 3). We then azimuthally extracted the

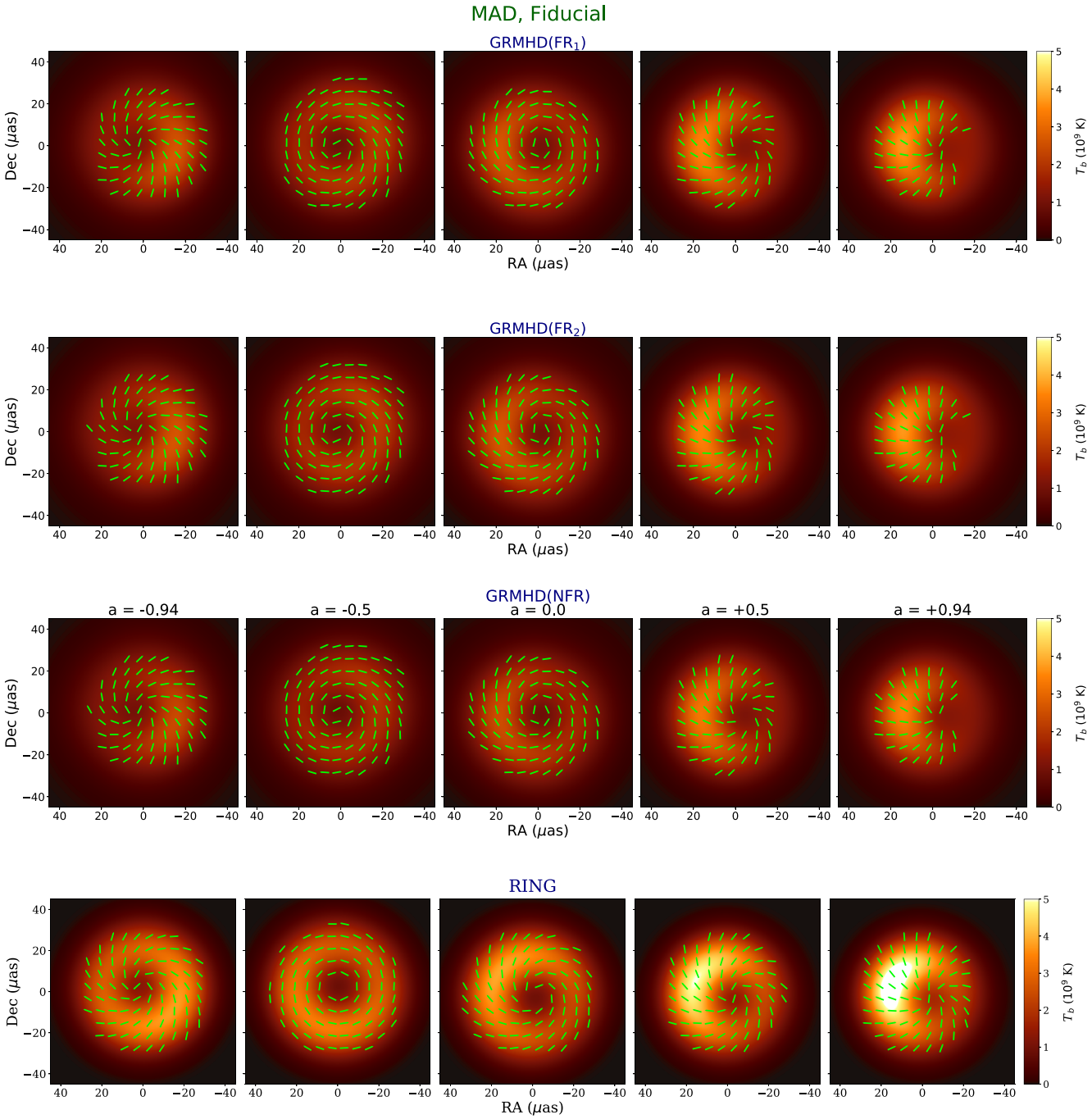

Figure 1. Time-averaged images of MAD models for the Fiducial case with $R_{\rm high} = 20$ and $R_{\rm low} = 1$ with different BH spins, $a = (-0.94, -0.5, 0.0, +0.5, +0.94)$. The first two rows plot polarimetric images computed using the complete radiative transfer equation, with two orientations of the magnetic field polarity, either aligned with the disk angular momentum on large scales ($\rm FR_1$) or anti-aligned ($\rm FR_2$). In the third row, we switch off Faraday rotation in this calculation to study its impact on the linear polarization pattern, which is not very significant for these models. Finally, in the fourth row, we plot images derived from an analytic ring model with parameters chosen to match the GRMHD. This ring model reproduces the evolution of the twisty morphology as a function of spin by including evolution in the magnetic field structure, velocity field, and emission location (but not Faraday rotation) as input from GRMHD.

equatorial magnetic fields and fluid velocities from the simulation.

A series of coordinate transformations were performed to convert the GRMHD output into a suitable ring model input. The fluid velocity is reported in a local inertial frame oriented along the FMKS coordinate axis, (see Appendix F of Wong et al. (2022) for a definition), while the magnetic field is extracted from GRMHD as a three-vector in the fluid frame. These quantities were used to construct a four-velocity and magnetic field four-vector as defined in Gammie et al. (2003), which was transformed to Boyer–Lindquist coordinates. Finally, we constructed the necessary four vector quantities for the ring model by transforming from Boyer–Lindquist to the equatorial ZAMO frame with the appropriate tetrads defined in Gelles et al. (2021), and performing the required Lorentz boost to retrieve the magnetic field vector in the fluid frame.

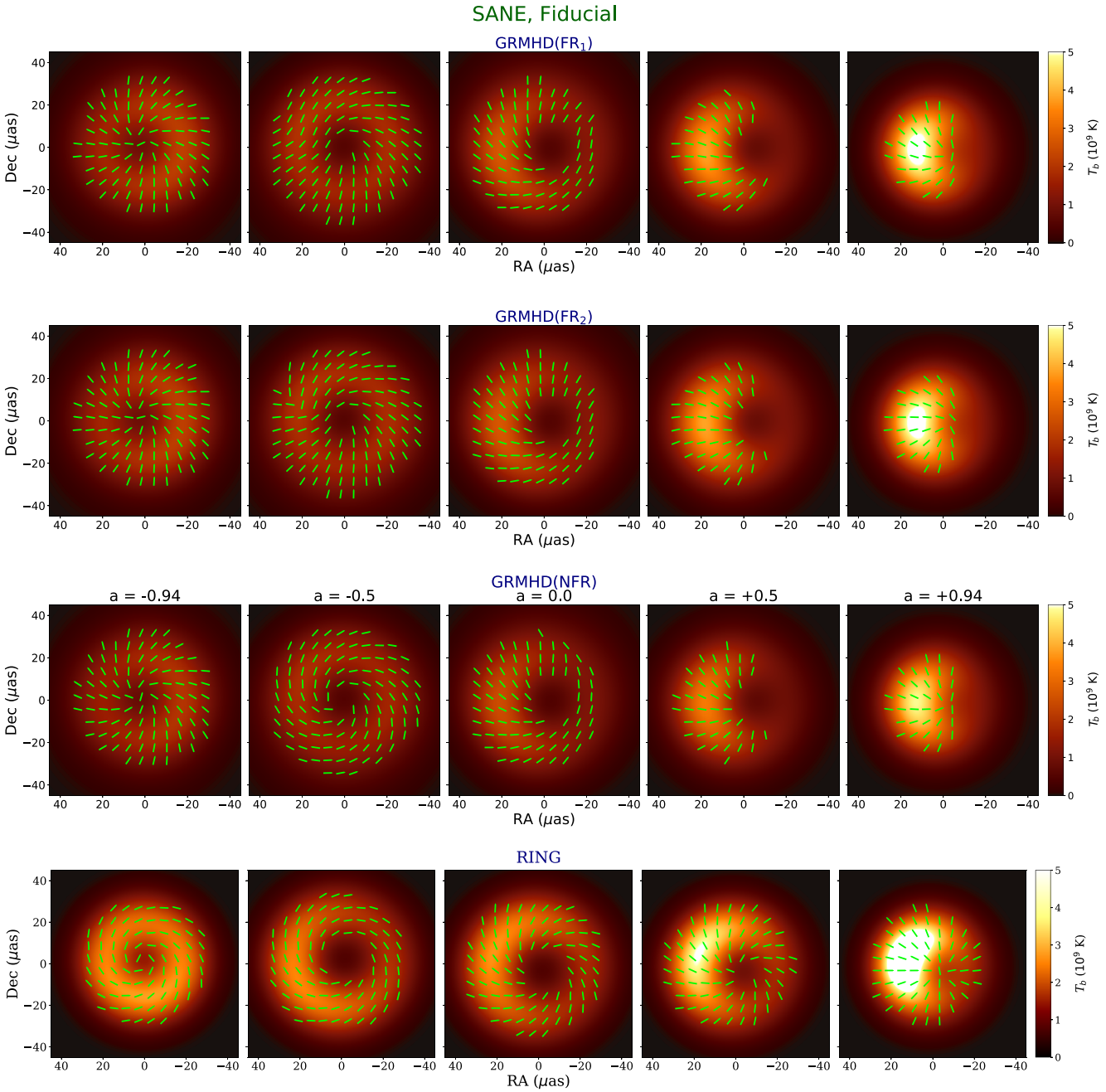

Figure 2. As Figure 1, but for our Fiducial SANE models. The impact of Faraday rotation is more significant due to their larger Faraday depths. While a ring model can broadly reproduce the nature of the morphology evolution as a function of spin, more deviations occur for our SANE models due to their more complicated emission geometries.

Table 1
The Time Average of Optical Depth (OD) and the Faraday Depth (FD) for the Fiducial (Fid) and the Faraday Thick (Thick) Cases for FR_1 and FR_2 Cases for MAD Simulations with $a = (-0.94, -0.5, 0.0, +0.5, +0.94)$

MAD Models	$a = -0.94$		$a = -0.5$		$a = 0.0$		$a = +0.5$		$a = +0.94$	
	FD	OD	FD	OD	FD	OD	FD	OD	FD	OD
Fid (FR_1)	2.1 ± 0.4	0.07 ± 0.03	2.6 ± 0.9	0.07 ± 0.03	2.1 ± 0.6	0.09 ± 0.03	1.7 ± 0.5	0.13 ± 0.04	0.9 ± 0.2	0.09 ± 0.04
Fid (FR_2)	2.1 ± 0.4	0.07 ± 0.03	2.6 ± 0.9	0.07 ± 0.03	2.1 ± 0.6	0.09 ± 0.03	1.7 ± 0.5	0.13 ± 0.04	0.9 ± 0.2	0.09 ± 0.04
Thick (FR_1)	360 ± 71	0.83 ± 0.33	433 ± 102	0.76 ± 0.28	386 ± 81	0.82 ± 0.30	405 ± 125	1.34 ± 0.45	176 ± 58	1.06 ± 0.40
Thick (FR_2)	360 ± 71	0.83 ± 0.33	433 ± 102	0.77 ± 0.28	387 ± 81	0.83 ± 0.34	406 ± 126	1.35 ± 0.45	176 ± 58	1.07 ± 0.40

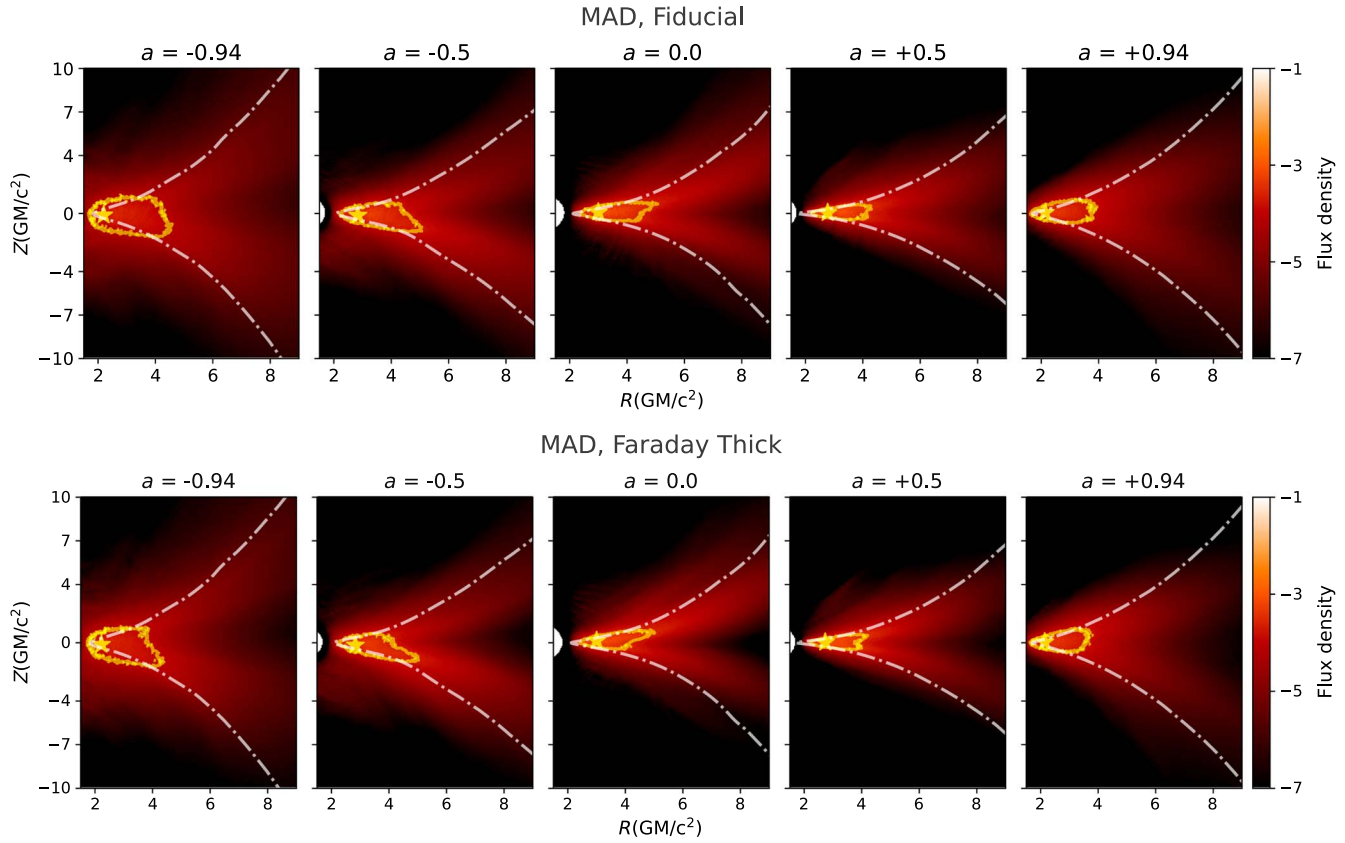

Figure 3. Azimuthal and time-averaged emissivity densities for our Fiducial (top) and Faraday Thick (bottom) MAD simulations. The yellow contour surrounds the region within which the top 30% of the emission is localized, while the gold star marks the single chosen emission location used for extracting the magnetic and velocity fields for the ring model. Dashed–dotted white lines indicate the $\sigma = 1$ contour. In each row, from the left to right, we increase the BH spin in the interval $a = (-0.94, -0.5, 0.0, +0.5, +0.94)$. Our MAD models, even those with large $R_{\rm high}$ and $R_{\rm low}$ are characterized by a ring of emission in the midplane.

Table 2
The Time Average of Optical Depth (OD) and the Faraday Depth (FD) for the Fiducial (Fid) and the Faraday Thick (Thick) Cases for FR_1 and FR_2 Cases for SANE Simulations with $a = (-0.94, -0.5, 0.0, +0.5, +0.94)$

SANE	$a = -0.94$		$a = -0.5$		$a = 0.0$		$a = +0.5$		$a = +0.94$	
Models	FD($\times 10^3$)	OD	FD($\times 10^3$)	OD	FD($\times 10^3$)	OD	FD($\times 10^3$)	OD	FD($\times 10^3$)	OD
Fid (FR_1)	8.2 ± 2.5	0.05 ± 0.03	17.8 ± 3.0	0.06 ± 0.03	69 ± 47	1.0 ± 1.6	2.1 ± 0.5	1.4 ± 0.9	0.2 ± 0.05	1.1 ± 0.9
Fid (FR_2)	8.2 ± 2.5	0.05 ± 0.03	17.8 ± 3.0	0.07 ± 0.03	69 ± 47	1.0 ± 1.7	2.2 ± 0.5	1.5 ± 0.9	0.2 ± 0.05	1.1 ± 0.9
Thick (FR_1)	267 ± 88	0.38 ± 0.15	657 ± 101	0.28 ± 0.08	4114 ± 2789	0.45 ± 0.11	1790 ± 425	6.0 ± 4.9	140 ± 46.8	9.1 ± 12.0
Thick (FR_2)	268 ± 88	0.38 ± 0.15	656 ± 101	0.28 ± 0.08	4128 ± 2798	0.45 ± 0.12	1878 ± 428	6.7 ± 5.6	140 ± 47	9.3 ± 12.3

3. Polarimetric Analysis and Results

In order to determine the origin of the linear polarization structure in our images, we perform an in-depth analysis of the GRMHD simulations at the location of peak emission. First, we locate the emissivity peak and sample the magnetic fields and velocity fields there. We input this information in an analytic ring model that treats Doppler boosting and lensing self-consistently (but does not include Faraday effects). We use this methodology to identify the mechanisms that determine $\angle\beta_2$, which describes the argument of β_2.

3.1. Time-averaged Polarized Images

Throughout our analysis, we mainly focus on the time-averaged images from different snapshots of a GRMHD simulation. That is, we are assuming that the turbulent character of the flow is stationary, and the source morphology may be characterized with a well-defined mean image. This notion appears to be consistent with the results of the multiyear M87* total intensity monitoring (Wielgus et al. 2020). Figures 1 and 2 present the time-averaged images of the GRMHD simulations and the geometrical ring model for the Fiducial case of MAD and SANE simulations, respectively. In each figure, the first two rows present images with aligned and anti-aligned magnetic fields (referred to as FR_1 and FR_2, respectively), followed by the case with no Faraday rotation (referred to as NFR) and the ring model (named as RING). Since the ring model does not include Faraday rotation, we are mostly concerned with comparing the NFR row with the RING

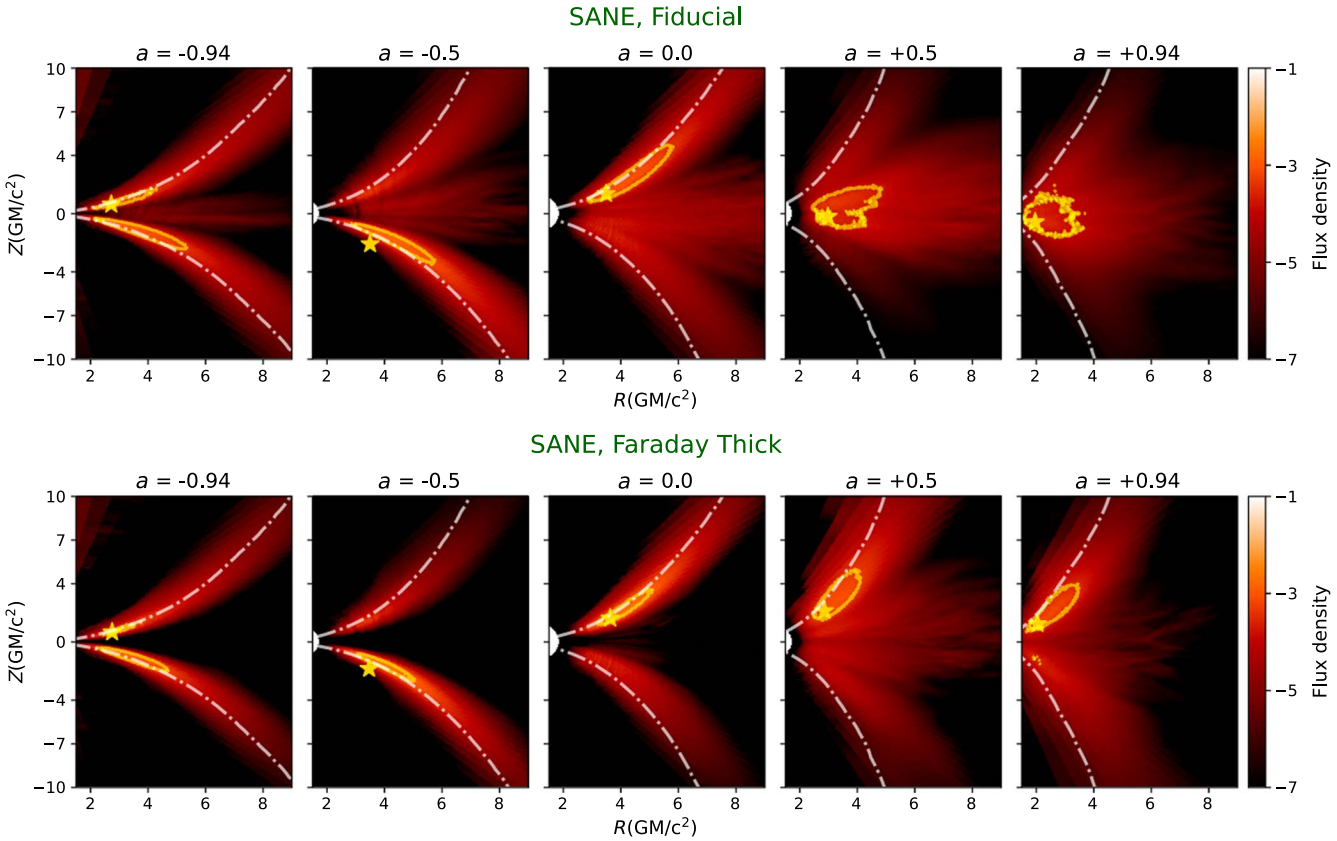

Figure 4. As Figure 3, but for our SANE simulations. Our SANE models have more complicated emission geometries and in some cases clearly exhibit multiple peaks of emission. Since we pick a single emission location to input into our ring model, we expect greater disagreement between GRMHD and analytic rings for our SANE models than their MAD counterparts. In each row, from the left to right we increase the BH spin in the interval $a = (-0.94, -0.5, 0.0, +0.5, +0.94)$.

row. In each row, from the left to right, we increase the BH spin in the interval $a = (-0.94, -0.5, 0.0, +0.5, +0.94)$.

From these plots, it is evident that the linear polarization pattern is not strongly affected by Faraday rotation. This itself is an important finding, since Faraday rotation and depolarization could have potentially randomized $\angle\beta_2$ in our models. Moreover, despite the abundance of simplifying assumptions made in constructing the ring models, they are remarkably successful at reproducing the overall handedness of the twisty polarization pattern especially in MAD simulations. SANE models, on the contrary, exhibit less agreement with the simple ring model. Consequently, the linear polarization pattern in MAD simulations can be explained by the magnetic field and velocity field at the emission peak, as input parameters in ring model, while its spin evolution can be attributed to frame dragging. This is explored in much greater detail in the following sections.

The azimuthally oriented EVPAs in low BH spins in MAD simulations are getting converted to radial ticks for high BH spins (both retrograde and the prograde spins) with more radial EVPAs for the prograde spins. Consequently, it is inferred that the ticks of the EVPAs might be directly linked to the BH spin and can be used to infer the spin. The azimuthal/radial pattern in MAD is getting slightly distorted in SANEs owing to the extra scrambling induced from the Faraday rotation. The radially oriented EVPAs in SANE prograde spins is also reflected in the ring model, though it is absent in the retrograde spins.

Since the electron-to-ion temperature ratio remains an important uncertainty in our models, this need not generically be the case. As constructed, Faraday rotation has a more significant effect in our Faraday Thick models. Their images are discussed in more detail in Appendix B.

3.2. Inferring the Optical Depth and Faraday Depth for Polarized Images

In the following, we infer the optical depth and the Faraday depth for images with different electron temperature profiles. Tables 1 and 2 present the mean and the standard deviation of the optical depth (OD) and the Faraday depth (FD) for the time-averaged GRMHD simulations for the Fiducial (Fid) and the Faraday thick (Thick) cases with FR_1 and FR_2 models for MAD and SANE simulations with $a = (-0.94, -0.5, 0.0, +0.5, +0.94)$, respectively. It is inferred from the tables that both of the OP and the FD are higher for the Faraday Thick case than the Fiducial case. Furthermore, while the FD is prominently higher in SANE simulations compared with the MADs, the OD is almost the same between MAD and SANEs for the retrogrades while it is higher in SANEs for the prograde cases.

3.3. Quantifying the Emission Location in GRMHD Simulations

As described in Section 2.2, we construct for each snapshot a 3D map of the emission location, which is then averaged over the time and azimuth to identify the r and z coordinates of the emission peak. In Figures 3 and 4, we plot the azimuthal and the time averages (see Section 3.1 for more details). Specifically, we identify the region containing the top 30% of

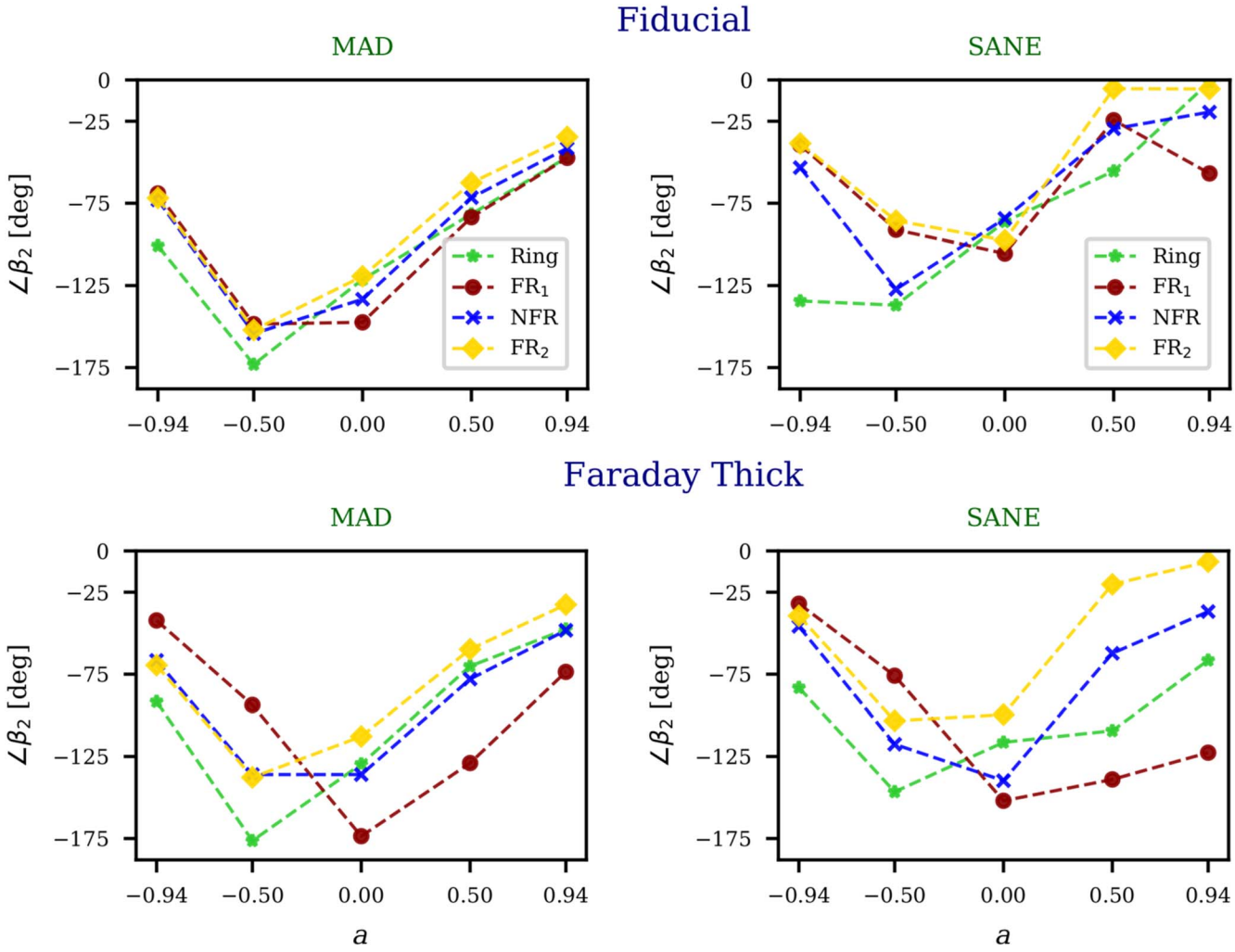

Figure 5. $\angle\beta_2$ for different GRMHD simulations and the ring model. FR_1, FR_2, NFR, and the ring model are marked with red circles, yellow diamonds, blue crosses, and green stars, respectively. The top row plots our Fiducial models, while the bottom row plots our Faraday Thick models. The left column plots our MAD models, while the right column plots our SANE models. A simple analytic ring given the appropriate velocity and magnetic fields does a remarkable job at reproducing $\angle\beta_2$ of our Fiducial MAD models. In other models, the differences between the NFR and $FR_{1,2}$ points reveal a stronger impact of Faraday rotation.

the emission, outlined in white. Marked with a gold star, we also present the chosen emission location as appropriate in the ring model. Tsunetoe et al. (2022a, 2022b) showed that the dominant emission location differs between the total intensity, the linear polarization, and the circular polarization. More specifically that the total intensity is mostly originated from the jet base while the linear polarization comes from the downstream of the jet and the circular polarization is maximum at the counter-jet. In our analysis, we use a mixed method, where we identify the top 30% of emission based on the intensity and mark them in Figures 3–4, while we fix the emission location, indicated with a star in Figures 3–4, such that the inferred $\angle\beta_2$ from the ring model gets as close as possible to the results of the GRMHD models.

We find that the emission of our Fiducial MAD models is concentrated in the midplane. Meanwhile, SANE simulations reveal a more complicated emission geometry (see also Event Horizon Telescope Collaboration et al. 2019e). In the Fiducial case, the emission of prograde models is mostly located in the midplane, but emission becomes more jet dominated in the other cases. Several of the SANE models are clearly not well described by a single ring. In the Faraday Thick SANE case, disk emission is further suppressed, moving more emission into the jet sheath. In conclusion, while the emission location is robust in MADs against changing the electron temperature, it depends on the details of the electron distribution in SANE simulations.

3.4. $\angle\beta_2$ as a Function of Spin

In analyzing distributions of the complex β coefficients of GRMHD simulations, Palumbo et al. (2020) point out an interesting dependence of $\angle\beta_2$ on the SMBH spin. We reproduce this result and plot both the Fiducial and Faraday Thick models (with magnetic fields aligned with the disk angular momentum; FR_1) in Figure 7. The differences in these distributions between aligned and anti-aligned magnetic fields are discussed in Appendix D. We find that most models exhibit relatively localized peaks of $\angle\beta_2$, even among our Faraday Thick models. Fortunately, Faraday rotation does *not* randomize $\angle\beta_2$ for a given snapshot. We find that our prograde SANE models are poorly localized, however. This is because they exhibit very low $|\beta_2|$ as written at the top right of each panel, and thus their $\angle\beta_2$ is not very meaningful. As discussed in Event Horizon Telescope Collaboration et al. (2021b), even though the retrograde SANEs exhibit a high Faraday depth, this

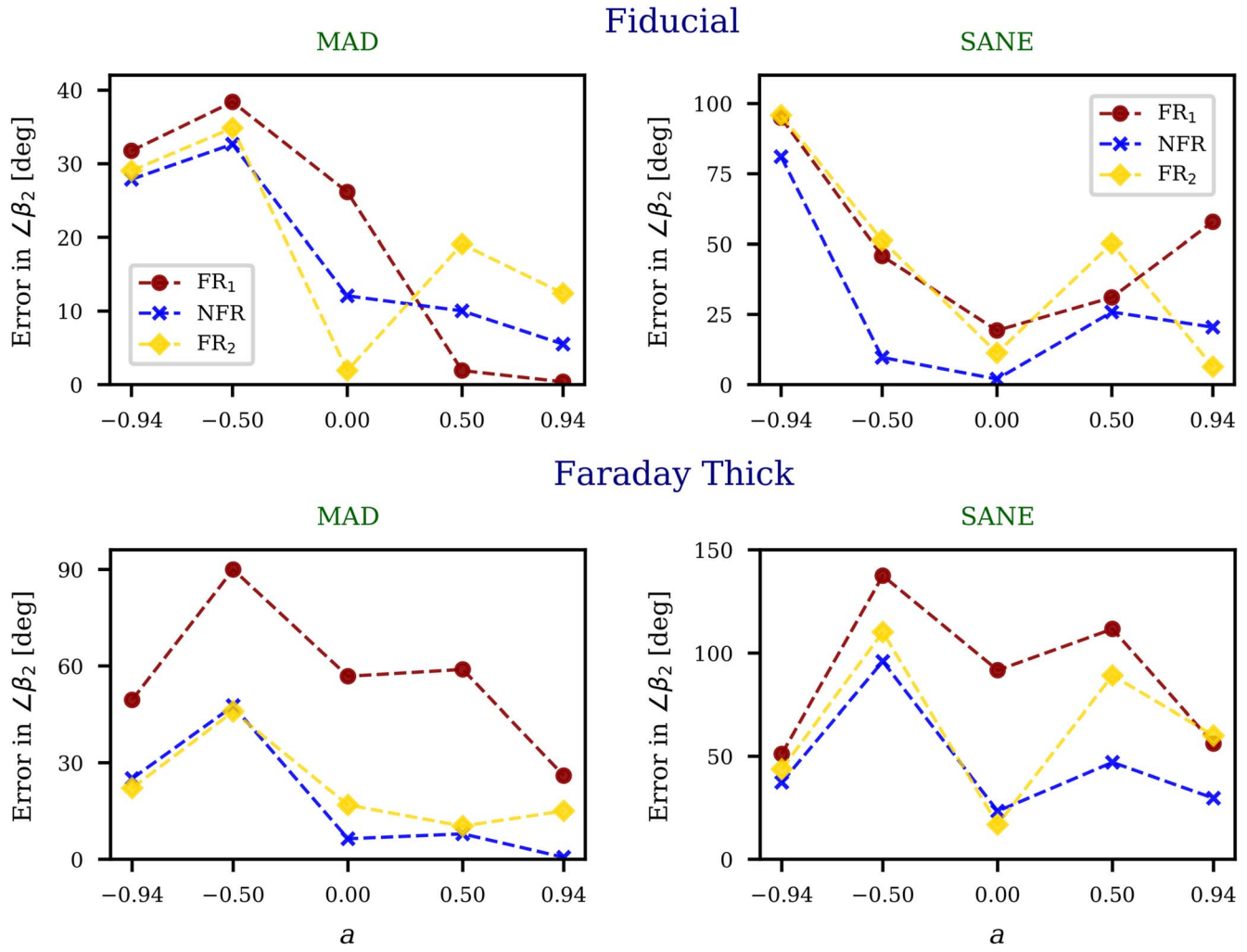

Figure 6. The error in the $\angle\beta_2$ for different GRMHD simulations compared with the ring model. FR$_1$, FR$_2$, and NFR are marked with red-circle, yellow-diamond and blue-cross , respectively. The top/bottom panels show the Fiducial/Faraday Thick cases, respectively. The left(right) panel show the MAD(SANE) simulations. Since Faraday rotation is not included in our simple ring model, it naturally produces the smallest errors when compared to the NFR cases.

Faraday depth does not affect forward-jet emission that is in front of the Faraday screen. Finally, while outside the scope of this paper, it is clear that the width of these distributions varies in interesting ways among these different models, which can be constrained by continued monitoring of M87*.

Here we compute the $\angle\beta_2$ in various GRMHD simulations, comparing them against the geometrical ring model. From the GRMHD part, we infer the phase of β_2 for FR$_1$, FR$_2$, and NFR, while from the ring side, we compute the $\angle\beta_2$ by choosing a few different locations with a high percentage of emission, fixing the magnetic and velocity fields in one final location where the inferred $\angle\beta_2$ from the ring model is the closest to the NFR case. The chosen place is then marked with gold stars in Figures 3 and 4.

Figures 5 and 6 present the $\angle\beta_2$ and the error in $\angle\beta_2$ in different GRMHD simulations and the ring model, respectively. In the top panel, we present the Fiducial case while in the bottom, we show the Faraday Thick case. In each row, the left/right panel presents the MAD/SANE case. From the plots, it is inferred that:

1. Overall, MAD simulations establish better agreement with the ring model than do the SANE simulations.
2. The level of the model agreements is higher in the Fiducial case compared with the Faraday Thick scenario. Furthermore, FR$_1$ and FR$_2$ are more similar in the former case than in the latter one. This is expected as the Faraday rotation is more prominent in the Faraday Thick case than the Fiducial case.
3. In the Faraday Thick case, the anti-aligned magnetic field, FR$_2$, gets closer to the NFR case than the aligned magnetic field.
4. Finally, it is seen that the $\angle\beta_2$ is directly linked to the BH spin. Consequently, we argue that the $\angle\beta_2$ in MAD and SANE simulations can be used to infer the BH spin.

3.5. Main Drivers of β_2

Here we explore different drivers of the ticks in EVPAs. The most key drivers of the EVPAs include plasma boost, gravitational lensing, and the magnetic field geometry. While the first two players are easier to probe individually, we may not turn off the magnetic field as it washes out the β_2 entirely. Owing to this, in what follows, we directly explore the impact of the plasma boost as well as the gravitational lensing, while indirectly estimating the importance of the magnetic field based

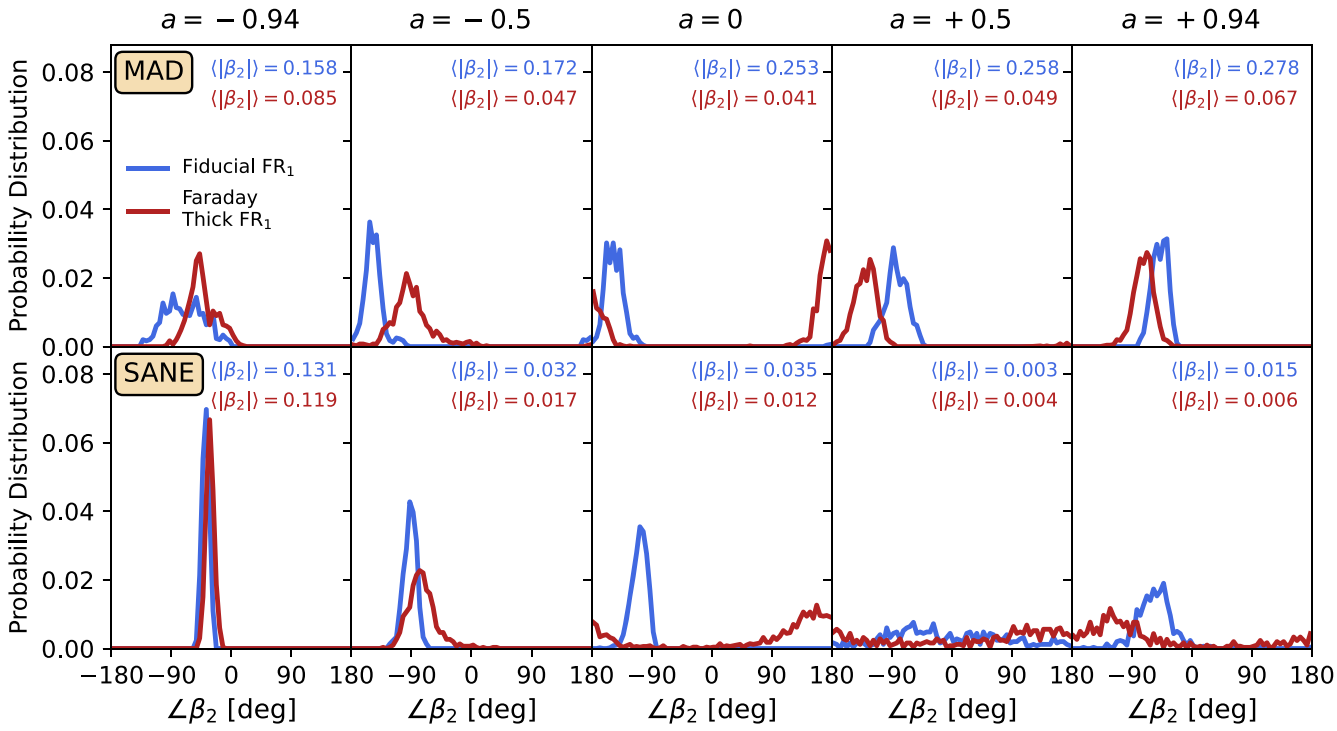

Figure 7. Distributions of $\angle\beta_2$ in our models. Fiducial models are shown in blue while Faraday Thick models are shown in red. At the top of each panel, we write the average amplitude of the β_2 mode as well. For models with $\langle|\beta_2|\rangle \gtrsim 0.1$, we find that these peaks are generally well localized. For some SANE models with scrambled $|\beta_2|$, $\angle\beta_2$ is randomized and carries little information.

on the deviations of EVPA ticks from their original values when we turn off the boost or the gravitational lensing.

3.5.1. Influence of Plasma Boost on β_2

The main role of the plasma boost factor can be traced by turning off the β in the ring model. The blue-crossed dashed lines in Figure 8 present the $\angle\beta_2$ in the absence of the boost factor. From the plot, it is inferred that, in MAD simulations, the deboosted lines generally follow the main trends in the $\angle\beta_2$, as is shown with green-starred dashed lines. SANEs, on the other hand deviate slightly from the main trend at low-retrograde spins, while they show a more reasonable behavior at higher spin cases. In conclusion, while the plasma boost is one of the players in driving the $\angle\beta_2$, it is not the key driver!

3.5.2. Impact of Gravitational Lensing on β_2

Next, we analyze the influence of the gravitational lensing on the EVPA ticks by scaling the BH mass down by a large factor, in our case, by a factor of 1000, and scaling up all coordinates by the same factor in order to preserve the angular size of the image. By placing emission at large radii in gravitational units, the impact of lensing is removed completely, altering the observed intensity and polarization by changing the angle of emission of geodesics that ultimately land at the observer screen. The impact of lensing is necessarily greatest in high-inclination models, while here we consider only nearly face-on models. Among these low-inclination models, these changes will have greater impact in models with large fluid velocities (where Doppler effects increase angular dependence of emitted intensity) and in models with larger variation in $\boldsymbol{k} \times \boldsymbol{B}$ across the image.

The plus-gray-dashed line in Figure 8 illustrates the impact of delensing on $\angle\beta_2$. From the plot, one can infer that, in MAD retrograde and low prograde spins, the delensed lines lie very close to the full ring models, while the high-spin prograde cases show a substantial deviation from the original ring model. Furthermore, the delensed cases in SANE simulations follow the same trends as in deboosted ones, meaning that both of these effects are not the main drivers in $\angle\beta_2$.

3.5.3. Influence of Magnetic Field Geometry on the β_2

Having found that boosting and lensing play relatively minor roles in driving $\angle\beta_2$, we now investigate the magnetic and the velocity fields at the emission location to elucidate trends with the BH spin. Figure 9 presents the absolute value of the normalized components of the magnetic field (top row) as well as the velocity field (bottom row) for our Fiducial model (solid lines) as well as the Faraday Thick case (dashed lines). From the plot, it is evident that the radial and azimuthal components of the B and V fields show a clear trend with the BH spin. In comparison, the polar components (vertical, when sampling the midplane) remain insignificant in comparison at the peak of the emitting region. Furthermore, in MAD simulations, this trend is not sensitive at all to the electron temperature, while in SANE simulations there is a very little dependence on the electron temperature in prograde spins. Note that since the magnetic field and velocity field are GRMHD primitives, any change as a function of electron temperature corresponds to a change in the peak of the emitting region. Consequently, we conclude that the combination of the B and V fields at the emission location might be very informative in constraining the BH spin.

Figure 10 presents the $\angle(|B_i/B_r|)$ (top row) and $\angle(|V_i/V_r|)$ (bottom row) with $i = (\theta, \phi)$ as a function of the BH spin. In

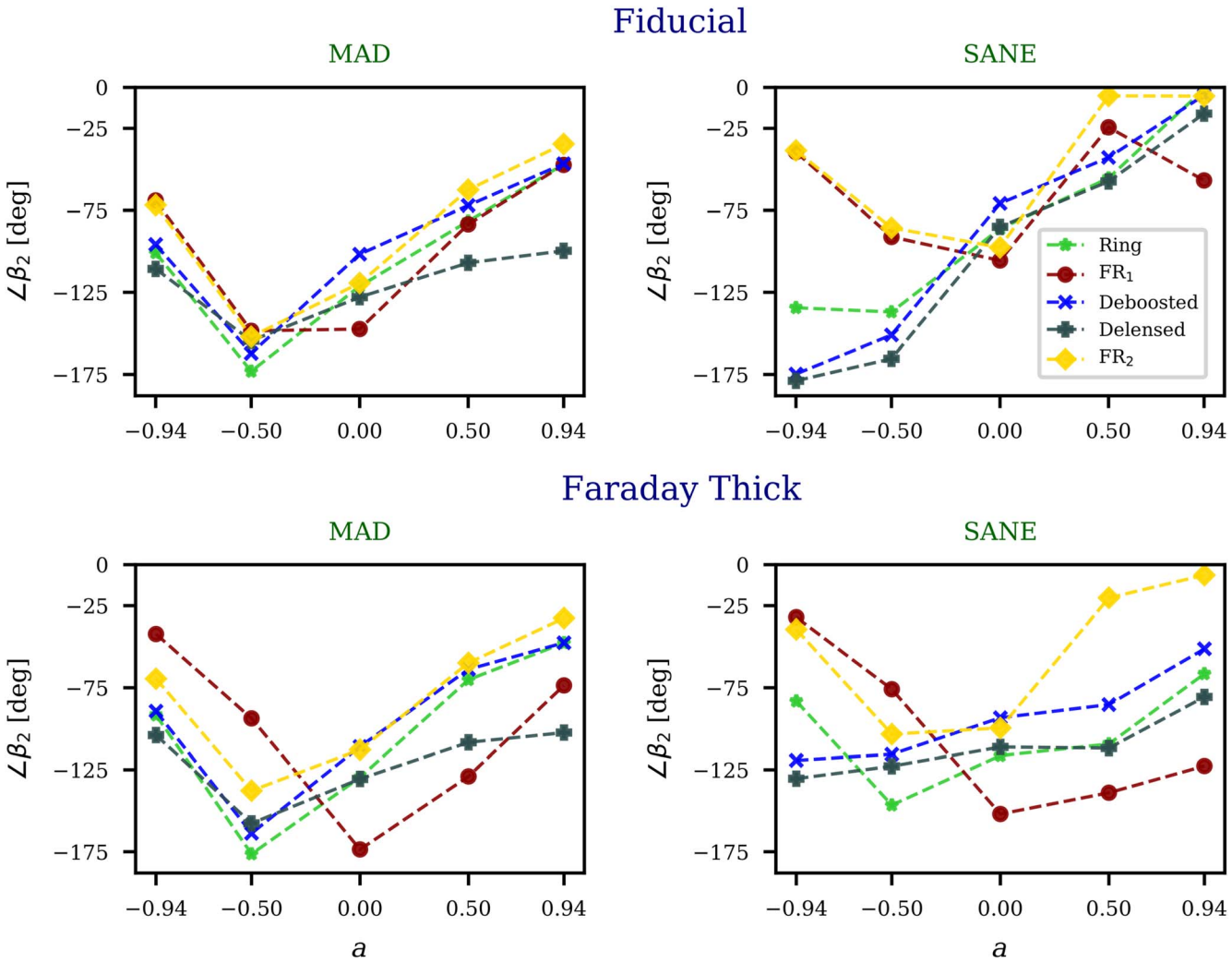

Figure 8. The impact of the plasma boost and the lensing on the phase of β_2. Doppler boosting and lensing both have mild effects on $\angle\beta_2$, but do not drive its evolution with spin.

each row, the left (right) panel shows the MAD (SANE) models. The solid (dashed) lines show the Fiducial (Faraday thick) cases. There is a clear trend of the aforementioned quantities with the BH spin. The trend is clearer for the azimuthal component than for the polar component. Both MAD and SANE simulations show similar behavior for each of the above quantities. For instance, in both cases, $\angle(|B_\phi/B_r|)$ has a turnover behavior in which the angle is first decreasing and then enhancing in the prograde regime, though the exact turnover point is not the same in MAD and SANE simulations. $\angle(|V_\phi/V_r|)$, on the other hand, establishes an enhancing pattern in both cases, though the slope of the enhancement is not the same in MAD and SANE.

These trends are naturally explained in the context of frame dragging of magnetic field lines. A generic helical pattern develops in disk-fed accretion flows from flux freezing and frame dragging (e.g., Semenov et al. 2004; Ricarte et al. 2021). First, we find that higher prograde spin values result in higher azimuthal velocities, as expected. This becomes reflected in the image as more Doppler boosting and thus greater asymmetry. More importantly, the magnetic field grows more tangential as spin increases, in either the prograde or retrograde cases. The exact ratio should depend on exactly the radius at which the emission peaks. Ricarte et al. (2022) explicitly showed the evolution of these components as a function of radius in a similar set of simulations, and in retrograde systems, a sign flip in this ratio can result in a similar sign flip in $\angle\beta_2$ with radius.

3.6. Impact of Faraday Rotation

As linear polarization travels through a magnetized plasma, Faraday rotation shifts the EVPA by an amount depending on the intervening density, temperature, and magnetic field. This effect could significantly impact $\angle\beta_2$ for two reasons. First, Faraday rotation imprints the line-of-sight direction of the magnetic field, rotating ticks counterclockwise if the field is pointed toward the observer and clockwise if the field is pointed away, which directly impacts $\angle\beta_2$. Second, large Faraday depths can lead to depolarization/scrambling, both along the line of sight and between neighboring regions. Our analytic ring model does not incorporate Faraday rotation, and thus it is important to determine to what extent it can impact our results.

To directly assess the affects of Faraday rotation, we compute images with Faraday rotation switched off (setting the coefficient $\rho_V = 0$) for each model. After computing $\angle\beta_2$ for images with Faraday rotation switched off and comparing with the images with Faraday rotation switched on as normal, we plot the distribution of

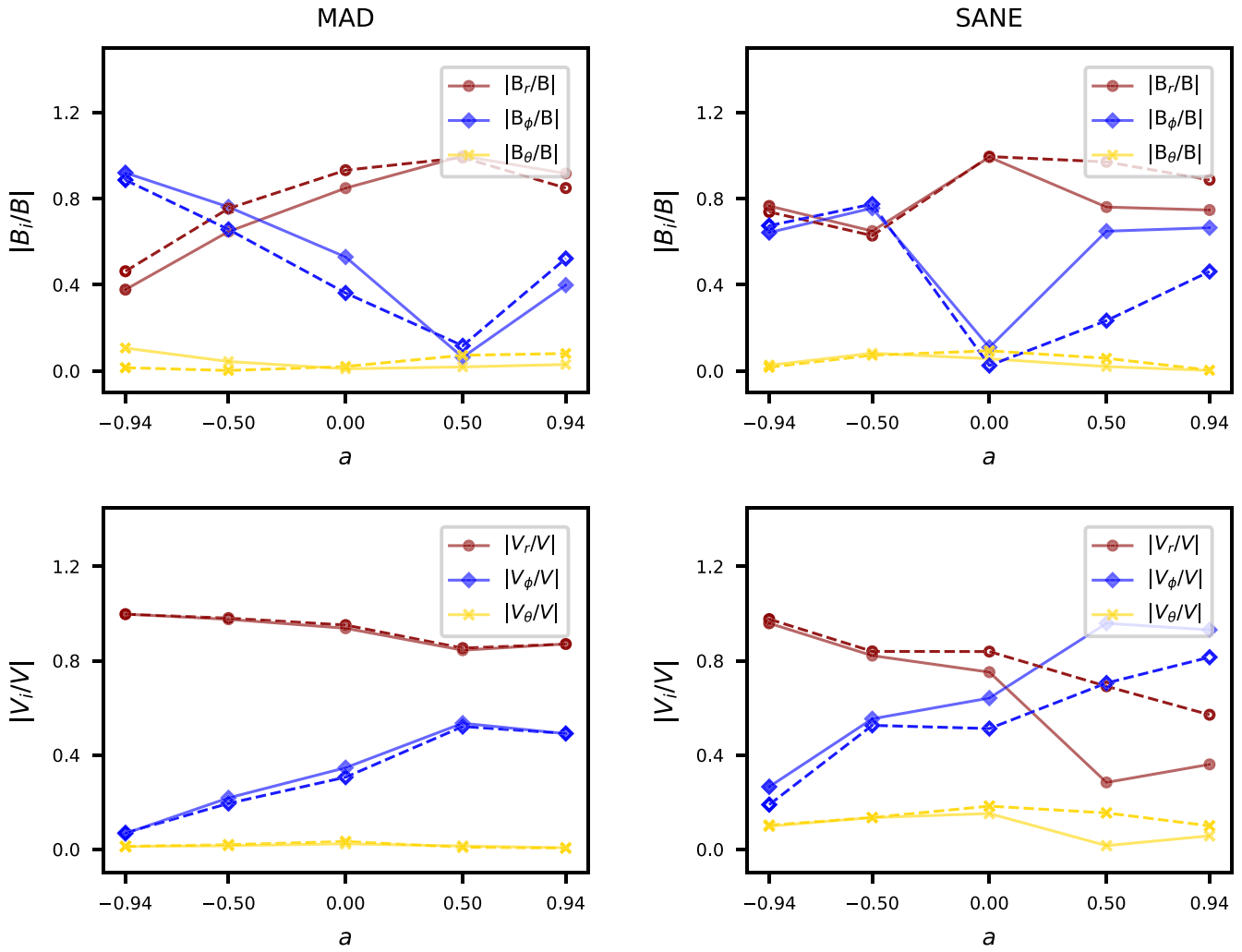

Figure 9. (Top) the $|B_i/B|$ vs. the BH spin, (bottom) $|V_i/V|$ as a function of the BH spin for MAD vs. the SANE simulation at the location of the emission for $R_{\rm high} = 20$ (filled symbols, solid lines) as well as $R_{\rm high} = 160$ (open symbols, dashed lines). Evidently, the r and ϕ field's components are dominant over the θ components for MAD simulations and are nearly the case for SANE simulations as well.

shifts in $\angle\beta_2$ induced by Faraday rotation in Figure 11. The blue lines show the Fiducial models, while the red lines present the Faraday Thick cases. For most models in the Fiducial set (and all of the MADs), we find that the impact of Faraday rotation is small, typically shifting $\angle\beta_2$ by roughly 10°. For most of the SANEs in the Fiducial set, this effect can be more significant. However, much of this can be explained by the fact that $|\beta_2|$ is low (written on the top right of each panel), and thus is not carrying much information to begin with.

We find an interesting pattern in the shifts due to Faraday rotation that differs between the prograde and retrograde models: retrograde models are preferentially shifted toward more positive values of $\angle\beta_2$ while prograde models are preferentially shifted toward more negative values. This pattern is consistent with a bias induced by the assumed direction of the vertical magnetic field, aligned here with the disk angular momentum on large scales. This is discussed in more detail in Appendix D.

In summary, we find that Faraday rotation fortunately usually does not randomize $\angle\beta_2$, even in some severely Faraday Thick models. However, it can impart a systematic shift in the distributions. This shift is small, approximately 10° for our Fiducial MAD models, but can potentially be much more significant for Faraday Thick and SANE models. We find an interesting signature of the polarity of the magnetic field that we discuss further in Appendix D.

In the set of Fiducial simulations considered in this paper, the poloidal field direction is arbitrarily assumed to be parallel with the BH spin. The field direction could equivalently have been oriented in the opposite direction without affecting the evolution of the GRMHD. Consequently, any image library including only poloidal fields aligned with the BH spin vector is incomplete.

4. Conclusions

We have performed an in-depth exploration of the origin of the "twistiness" of the EVPAs, quantified by the $\angle\beta_2$, in simulated, time-averaged polarized images of M87*. We used a simple ring model to take into account different contributions including the plasma Doppler boosting, gravitational lensing, and magnetic field geometry, in driving the ticks of EVPAs. We inferred the main location of the emission in various GRMHD simulations and read the magnetic and velocity fields at the emission location as key ingredients in our geometrical ring model. Our results can be summarized as follows:

1. Comparing the geometric ring model with the GRMHD simulations, it is inferred that MAD models in general

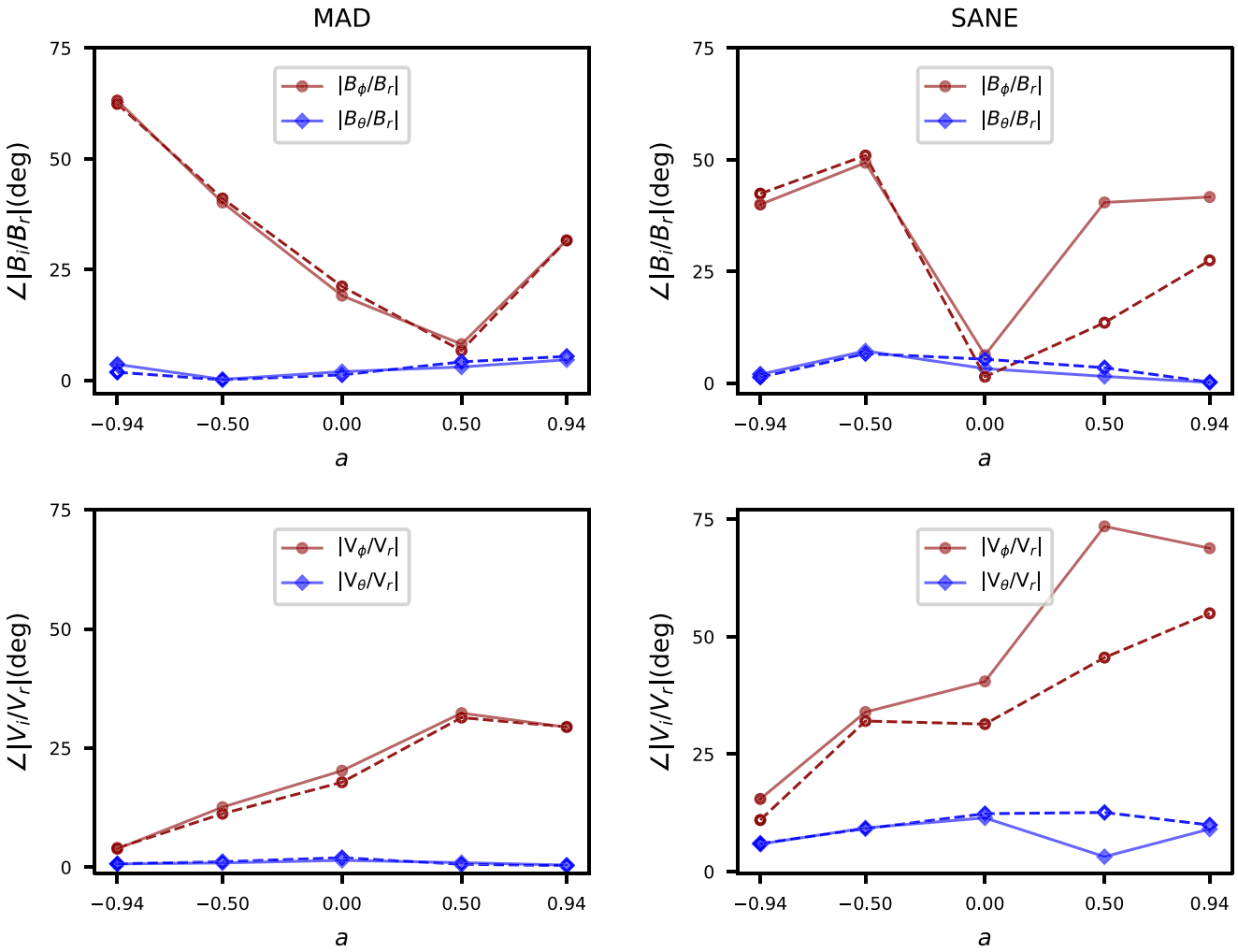

Figure 10. (Top) the $\angle(|B_i/B_r|) \equiv \arctan(|B_i/B_r|)$ vs. the BH spin, (bottom) $\angle(|V_i/V_r|) \equiv \arctan(|V_i/V_r|)$ with $i = (\phi, \theta)$ as a function of the BH spin for MAD vs. the SANE simulation at the location of the emission.

provide a better agreement with the ring model than do the SANE cases.

2. The Fiducial case shows a higher level of agreement than the Faraday Thick models, as expected, owing to the fact that the Faraday rotation is more important in the latter case than the former one.
3. $\angle\beta_2$ seems to be directly linked to the BH spin, therefore it may be possible to use the twistiness of the ticks of the linear polarization to the infer the BH spin.
4. Our analysis showed that among the drivers of the ticks of the EVPAs, the plasma boost and gravitational lensing provide a subdominant contribution in determining $\angle\beta_2$. Consequently, the magnetic field geometry predominantly drives the ticks of the linear polarization.
5. We have shown that there is a trend in the normalized amplitude of the radial and azimuthal components of the magnetic and velocity fields at the emission location with the BH spin. This is encouraging, as any future measurement of the magnetic field and the plasma velocity might be very informative about the BH spin. Consequently, we propose to use the next generation of the EHT (ngEHT) to look for the BH spin through a measurement of the B and V fields at the emission location.
6. We found that the impact of Faraday rotation on $\angle\beta_2$ is small for our Fiducial models. However, we noticed an interesting bias induced by the alignment versus anti-alignment of the vertical magnetic field direction with the BH spin. This bias becomes much more significant in the Faraday Thick models, which have relatively cooler electrons and increased Faraday depths compared to the Fiducial case. Future studies using libraries of model images from GRMHD should also include models where the magnetic field direction is flipped, which fortunately does not require additional GRMHD simulations.
7. Although we considered a wide range of models in this paper, we did not explore the impact of different initial conditions on trends in $\angle\beta_2$. Higher resolutions could also qualitatively alter the flow when the plasmoids form. Finally, different emission models including nonthermal models, positrons, and the tilted-disk models may also contribute in changing the results. We leave further explorations of the above cases to a future study.

Acknowledgments

It is a great pleasure to thank Peter Galison and Michael Johnson for very fruitful conversations. We are very grateful to the referee for very constructive comments. R.E. acknowledges support by the Institute for Theory and Computation at the Center for Astrophysics as well as grant numbers 21-atp21-

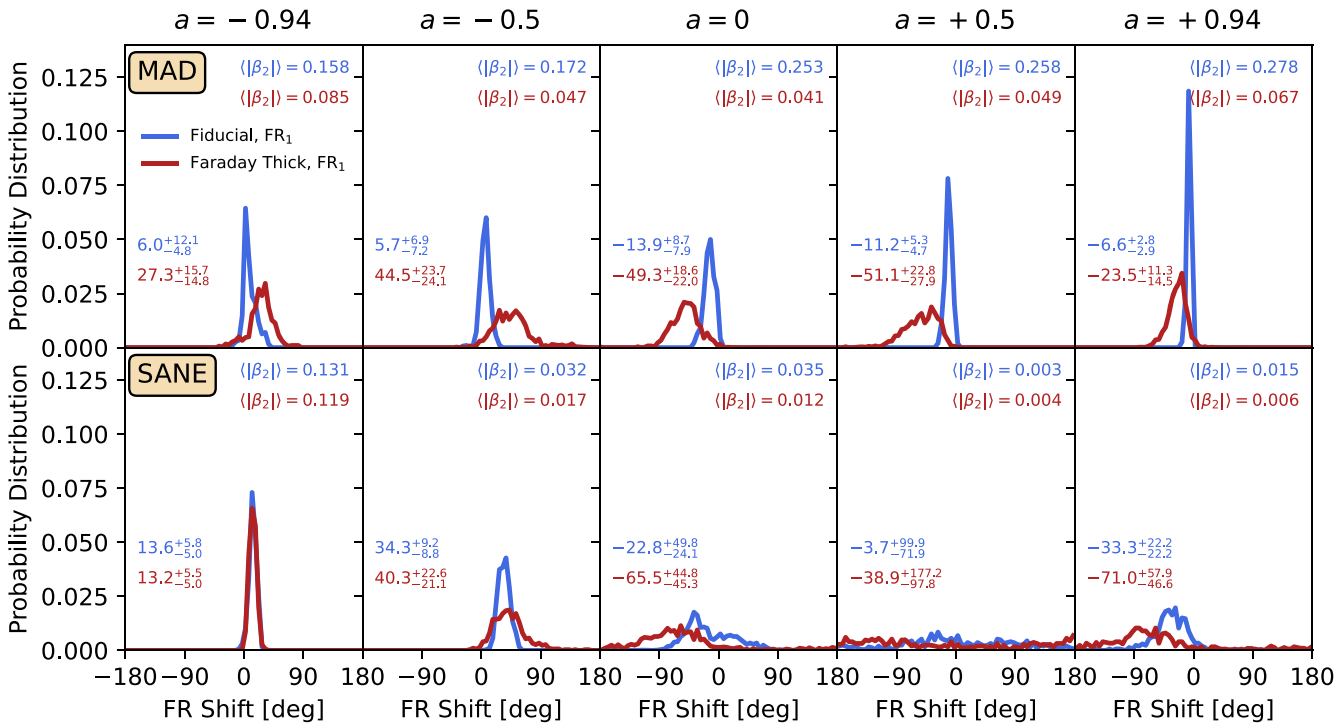

Figure 11. For each of the models, we compute the shift in $\angle\beta_2$ due to Faraday rotation and here plot the probability distribution of these shifts. At the top of each panel, we also write the average amplitude of β_2 to show how important the mode is for each model. The text in each panel quotes 16th, 50th, and 84th percentiles for these shifts. For models where $\langle|\beta_2|\rangle$ is significant ($\gtrsim$0.1), we find that these shifts are modest, demonstrating that Faraday rotation typically only has a small impact on β_2 for these models. However, Faraday rotation can cause a much greater shift in SANEs and our Faraday Thick models. We find an interesting bias induced by the assumed direction of the magnetic field. Retrograde models are preferentially shifted toward more positive values, while prograde (and spin 0) models are shifted toward more negative values due to the assumption that the vertical magnetic field is aligned with the outer disk angular momentum, which is reversed by construction in our retrograde models.

0077, NSF AST-1816420, and HST-GO-16173.001-A. We thank the supercomputer facility at Harvard University where most of the simulation work was done. G.N.W. gratefully acknowledges support from the Taplin Fellowship. A.R.R. and K.C. acknowledge support by the National Science Foundation under grant No. OISE 1743747. R.J.A. acknowledges the Future Faculty Leaders Postdoctoral Fellowship. This research was made possible through the support of grants from the Gordon and Betty Moore Foundation and the John Templeton Foundation. D.C. acknowledges the support of the black hole Initiative at Harvard University, which is funded by grants from the John Templeton Foundation and the Gordon and Betty Moore Foundation to Harvard University. A.C. was supported by Hubble Fellowship grant HST-HF2-51431.001-A awarded by the Space Telescope Science Institute, which is operated by the Association of Universities for Research in Astronomy, Inc., for NASA, under contract NAS5-26555. A.C. also gratefully acknowledges support from the Princeton Gravity Initiative. This work was also supported by the National Science Foundation grants AST-1935980 and AST-2034306 and the Gordon and Betty Moore Foundation (GBMF-5278). The opinions expressed in this publication are those of the author(s) and do not necessarily reflect the views of the Moore or Templeton Foundations. F.R. was supported by NSF grants AST-1935980 and AST-2034306. I. M.-V. acknowledges support from the GenT program of Generalitat Valenciana (CIDEGENT/2018/021), MICINN Research Project PID2019-108995GB-C22 and the Astrophysics and High Energy Physics Programme by MCIN, with funding from European Union NextGenerationEU (PRTR-C17I1) and the Generalitat Valenciana through grant ASFAE/2022/018.

Software: matplotlib (Hunter 2007), numpy (van der Walt et al. 2011), scipy (Oliphant 2007), seaborn (Waskom et al. 2020), pandas (Reback et al. 2021), h5py (de Buyl et al. 2016).

Data Availability

Data directly corresponded to this manuscript and the figures is available to be shared on reasonable request from the corresponding author. The ray tracing of the simulation done in this work was performed using IPOLE (Mościbrodzka & Gammie 2018). We have used the library of IHARM simulations by Gammie et al. (2003) and Prather et al. (2021) from the standard library of 3D time-dependent GRMHD simulations performed in Event Horizon Telescope Collaboration et al. (2019e, 2021b).

Appendix A
σ Contours in The R versus Z Plane

As already discussed in the main text, we made the BH images using $\sigma_{\rm cut} = 1$. This means that all the regions with a $\sigma \geqslant 1$ should be considered with a bit of caution. In Figure 12, we present the color plot of $\log_{10}(\sigma)$ in the source R versus Z plane using the time-averaged GRMHD simulations of MAD (top) and SANE (bottom) rows, respectively. In each panel, the BH spin is increased in $a = (-0.94, -0.5, 0.0, +0.5, +0.94)$. Overlaid in each panel, we present the emission location with black star. From the plots, it is inferred that our emission location is fairly consistent with the $\sigma_{\rm cut} = 1$.

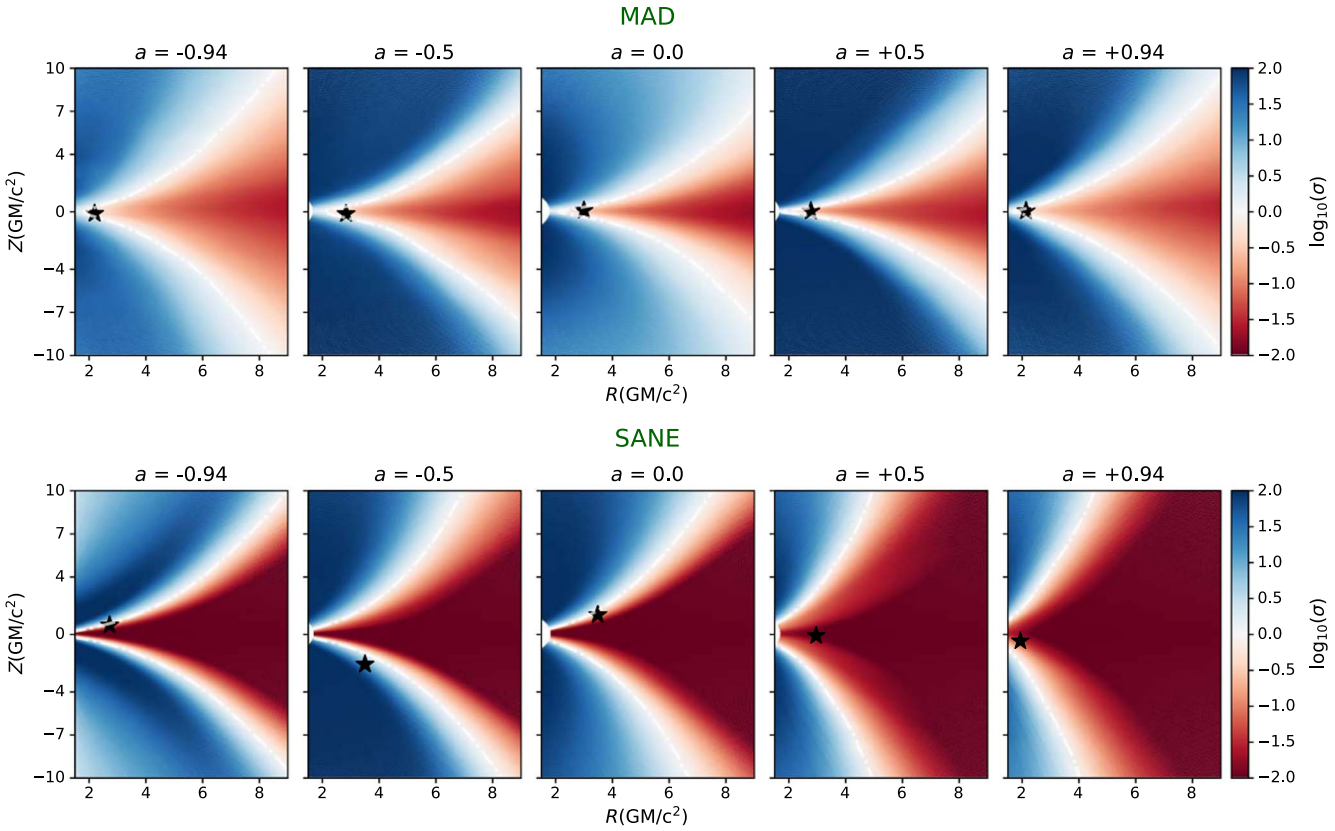

Figure 12. The color plot of $\log_{10}(\sigma)$ in the source R vs. Z plane for MAD (top) and SANE (bottom) simulations.

Appendix B
Averaged Images from Faraday Thick Model

Having presented the time-averaged images of the Fiducial case in Figures 1 and 2, here we focus on Faraday Thick models. Figures 13 and 14 present the time-averaged images for MAD and SANE models with different BH spins, respectively. Descending rows present FR_1, FR_2, NFR, and the ring model. Comparing these images with the Fiducial case, it is evident that the Faraday rotation is more important here than there. Consequently, the level of the agreement with the ring model diminishes in the Faraday Thick case than the Fiducial model. Overall, MAD simulations provide a better agreement to the geometrical ring model than the SANE ones. In both cases, the more radially oriented EVPAs at higher absolute BH spin, gets more azimuthally oriented in low/zero spin models.

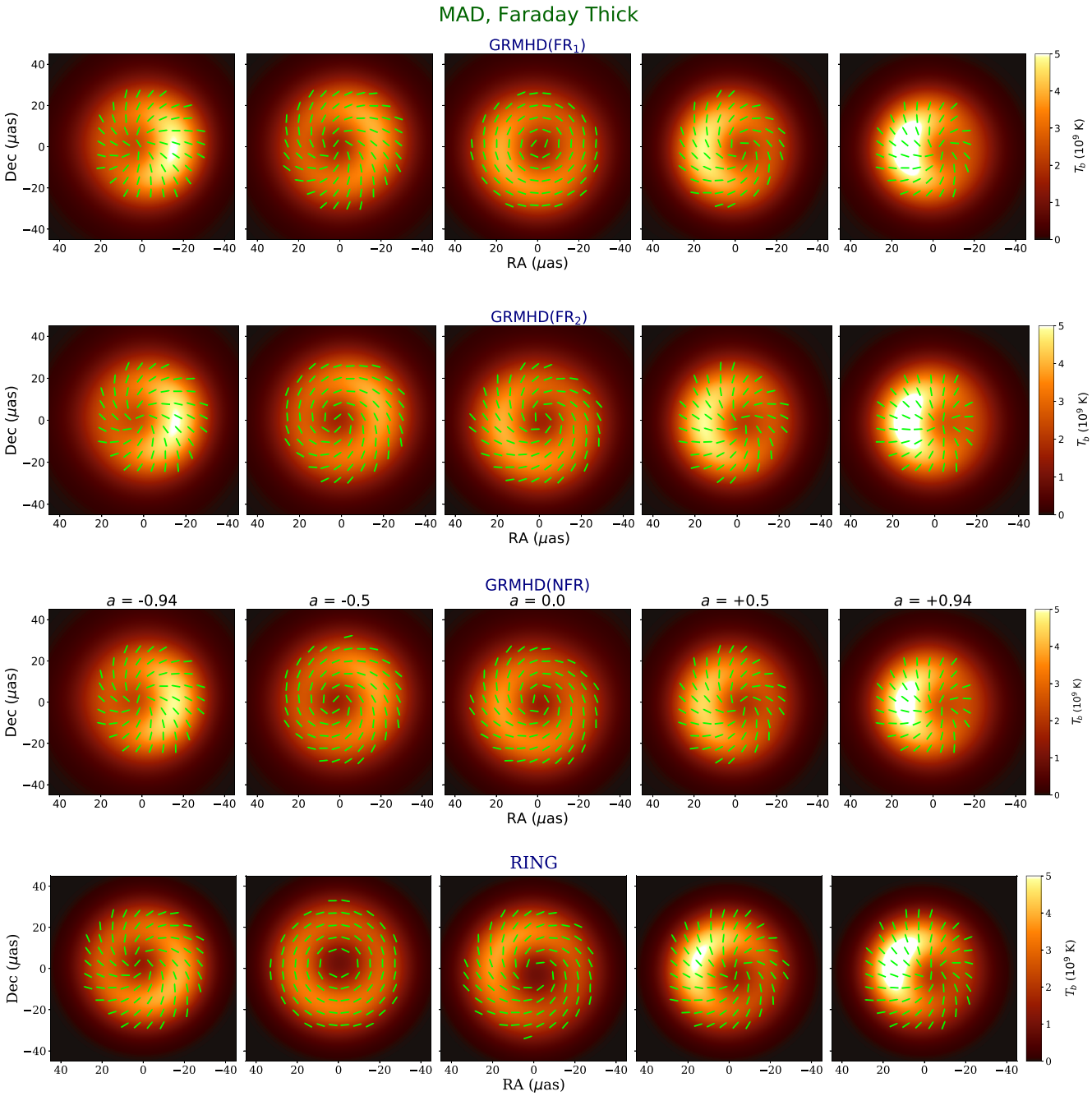

Figure 13. The averaged image of intensity from MAD simulation which are Faraday Thick with $R_{\rm low} = 10$ and $R_{\rm high} = 160$ with different BH spins represented in consecutive columns, $a = (-0.94, -0.5, 0.0, +0.5, +0.94)$. The green tick lines refer to the EVPAs.

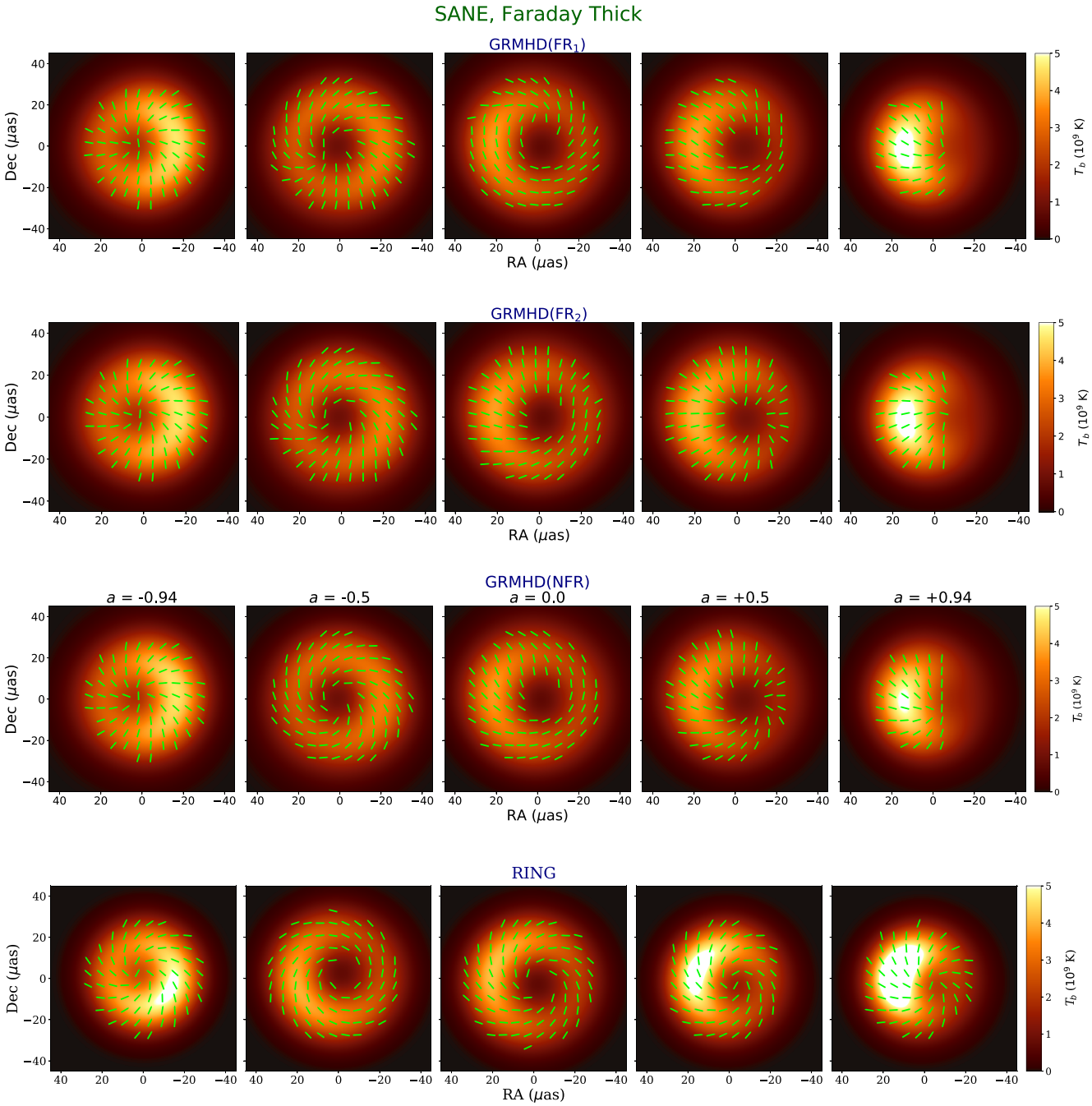

Figure 14. The averaged image of intensity from the case of SANE simulation with Faraday Thick associated with $R_{\rm high} = 160$ and $R_{\rm low} = 10$ with different BH spins represented in consecutive columns, $a = (-0.94, -0.5, 0.0, +0.5, +0.94)$. The green tick lines refer to the EVPAs.

Appendix C
Impact of The Deboosting and Delensing

To isolate different contributions in the ring model, in the following, we assess versions of the ring model in which either the plasma boost factor or the gravitational lensing term are turned off. The Fiducial and the Faraday Thick cases are considered separately. In order to diagnose the effects of Doppler beaming on the observed EVPA distribution, we utilize the ray-traced toy model while setting the fluid velocity to zero in Boyer–Lindquist coordinates. On the other hand, to study the contribution of the general relativistic lensing, we scale down the BH mass in the ray-tracing code while scaling the radius of emission in gravitational coordinates up, maintaining the same physical size of the emission and the same approximate angular size of the ring. Furthermore, we preserve the velocity structure of the simulation, effectively performing ray tracing in a flat spacetime (delensed test).

C.1. Fiducial Case

Here we analyze the Fiducial simulations. Figures 15 and 16 compare the polarized images from the ring model (top row) with the deboosted ring (middle row) and the delensed ring (bottom row) for models of MAD and SANE in the Fiducial case, respectively. From the plots, it is inferred that:

In MAD simulations, the brightness distribution of the original ring is very similar to the deboosted ring model. This is, however,

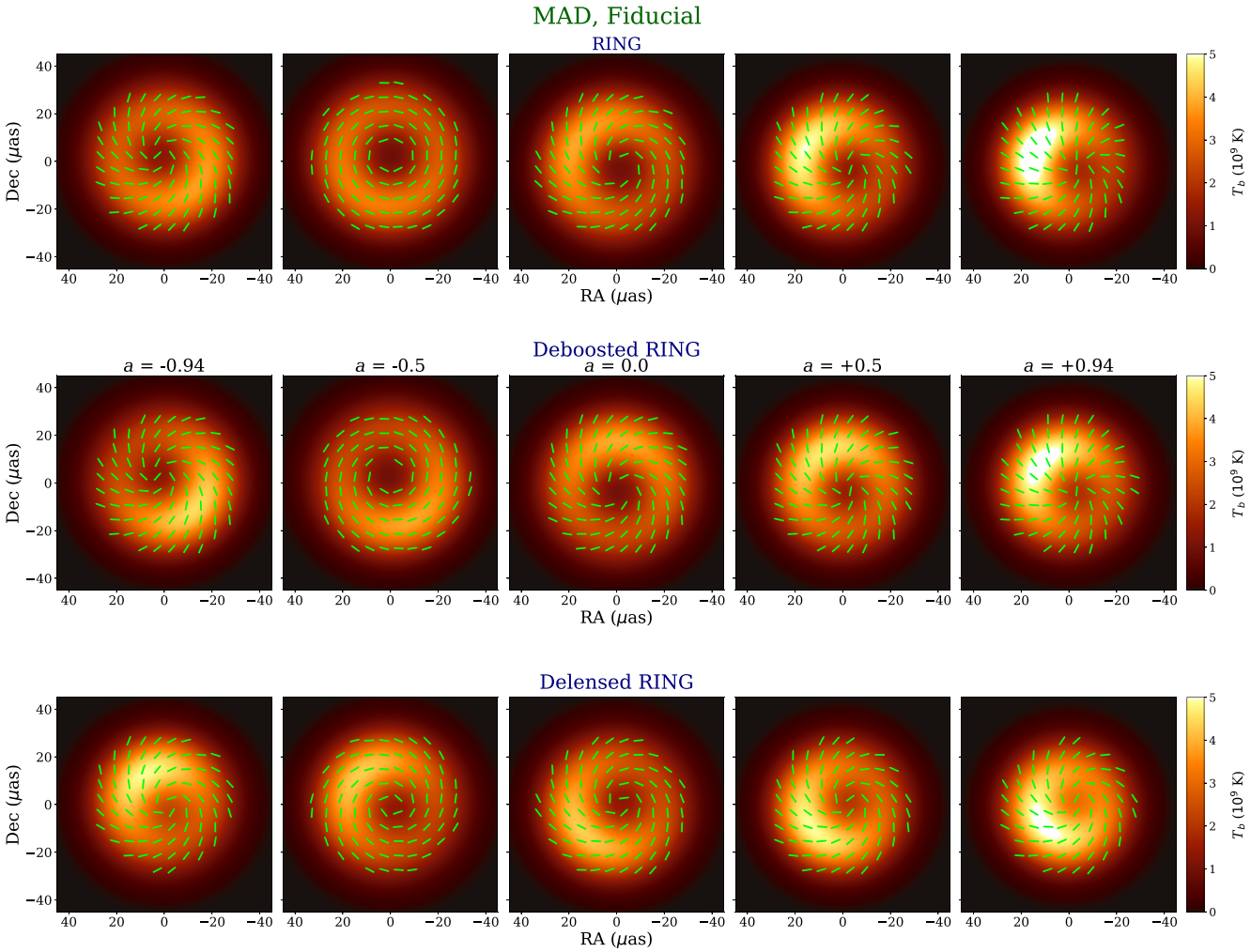

Figure 15. The impact of turning off the plasma boost as well as the lensing in the Fiducial case for MAD simulations. From the top row to the bottom one, we present the full ring, deboosted, and the delensed cases, respectively, with different spin values represented in consecutive columns.

not the case for the delensed ring model in which we see substantial differences between the brightness distribution of the original ring compared with the delensed ring model. The ticks of the EVPAs, on the other hand, seem more similar between different cases in MAD simulations. The details of the comparison between the ticks of EVPAs can be found in Figure 8.

In SANE simulations, the differences between the brightness distribution of the ring model (top row) and the deboosted ring (middle row) is more noticeable with more differences in the retrograde and zero spin than the prograde cases. The delensed ring model, on the other hand, shows more similarity to the ring model (top row) with an exception only for the case with $a = -0.94$. There are some levels of changes between the ticks of the EVPAs in all of these cases as well. We have quantified such differences in Figure 8.

C.2. Faraday Thick Case

Next, we study the Faraday Thick simulations. Figures 17 and 18 compare the polarized images from the ring model (top row) with the deboosted ring (middle row) and the delensed one (bottom row) for models of MAD and SANE in the Faraday Thick case, respectively. From the plots, it is inferred that:

In MAD simulations, both the brightness distribution of the deboosted ring model and the ticks of the EVPAs follows closely the behavior of the original ring model, which is quite similar to the above Fiducial case, as seen in Figure 15. The structure however is rather different in the delensed ring model. A more quantitative comparison between the ticks of the EVPAs can be found in the bottom row in Figure 8.

In SANE simulations, the distribution of the brightness in the deboosted case shows a bit less agreement with the original ring model than in MAD simulations. The ticks of the EVPAs also show slightly less agreement for retrograde spins. The brightness distribution of the delensed models show substantial differences compared with the original ring model. This behavior is quite similar to the Fiducial case, as shown in Figure 16. The details of the quantitative comparison between these models can be found in Figure 8.

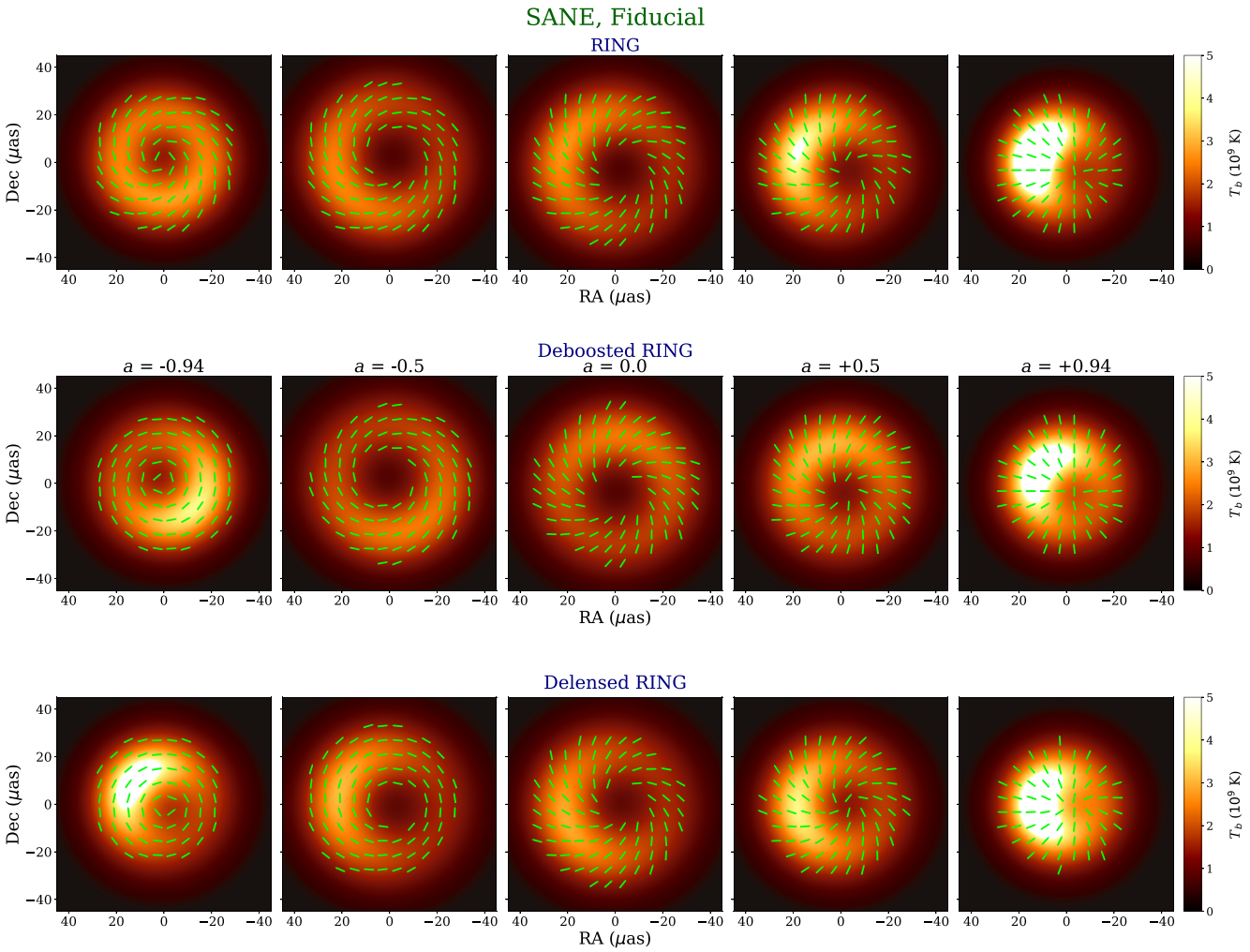

Figure 16. The impact of turning off the plasma boost as well as the lensing in the Fiducial case for SANE simulations. From the top row to the bottom one, we present the full ring, deboosted, and the delensed cases, respectively, with different spin values represented in consecutive columns.

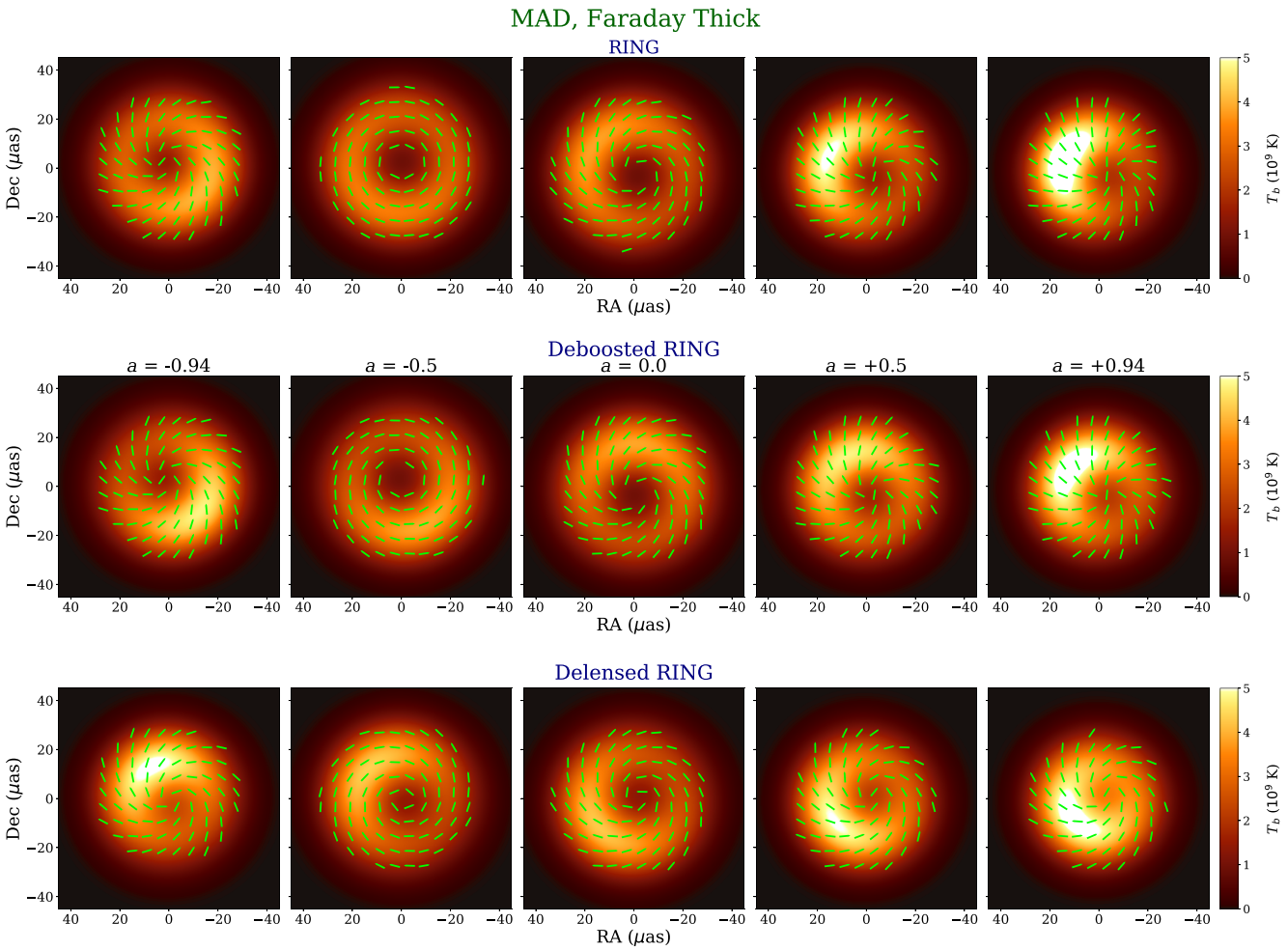

Figure 17. The impact of turning off the plasma boost as well as the lensing in the Faraday Thick case for MAD simulations. From the top row to the bottom one, we present the full ring, deboosted and the delensed cases, respectively, with different spin values represented in consecutive columns.

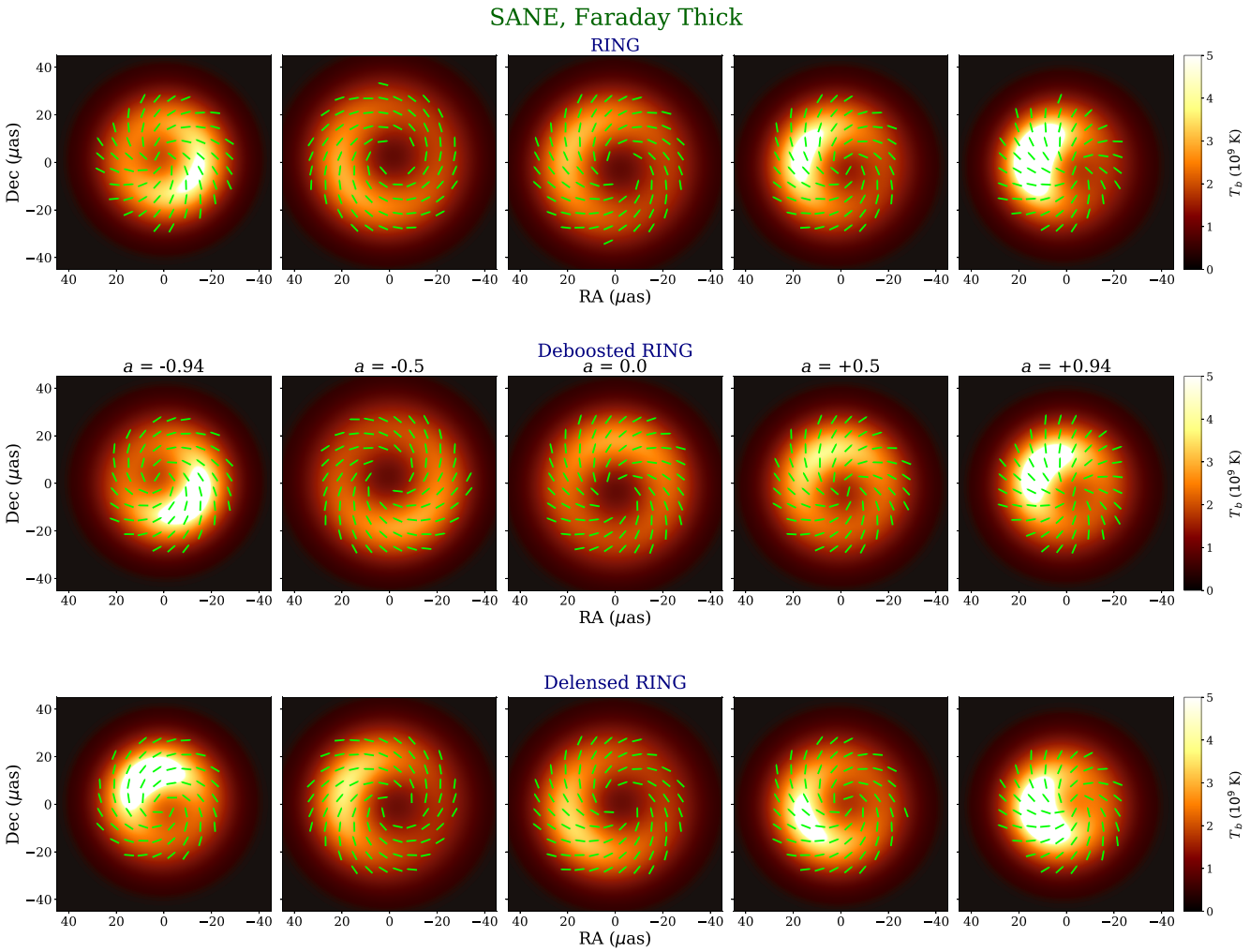

Figure 18. The impact of turning off the plasma boost as well as the lensing in the Faraday Thick case for SANE simulation. From the top row to the bottom one, we present the full ring, deboosted, and the delensed cases, respectively, with different spin values represented in consecutive columns.

Appendix D
Effect of the Magnetic Field Polarity

Throughout this work, we have considered two orientations of the magnetic field polarity, either aligned or anti-aligned with disk angular momentum on large scales. EHT science thus far has focused on models with the magnetic field aligned with the disk angular momentum. However, since the equations of GRMHD are invariant to a flip in the magnetic field direction, the same GRMHD snapshots can be ray traced using either magnetic field polarity. This has negligible impact on total intensity, but can alter both the linear and circular polarization structure. Depending on the model, flipping the magnetic field direction can result in a complicated change in the circular polarization structure, since intrinsic emission and Faraday rotation change sign, but Faraday conversion does not (Ricarte et al. 2021). In linear polarization, the direction of the field causes a systematic rotation of polarization ticks due to Faraday rotation, which directly impacts $\angle\beta_2$.

In Figure 19, we plot the distribution of changes in $\angle\beta_2$ upon flipping the field ($\angle\beta_2(\mathrm{FR}_2) - \angle\beta_2(\mathrm{FR}_1)$) on a snapshot-by-snapshot basis. As expected, the effect is stronger for models with more Faraday rotation. This flip induces positive shifts in $\angle\beta_2$ for prograde and spin 0 models and negative shifts in retrograde models because their poloidal magnetic fields are oriented in opposite directions by construction. We expect that the observable quantities sensitive to the magnetic field polarity are $\angle\beta_2$, circular polarization, and rotation measure.

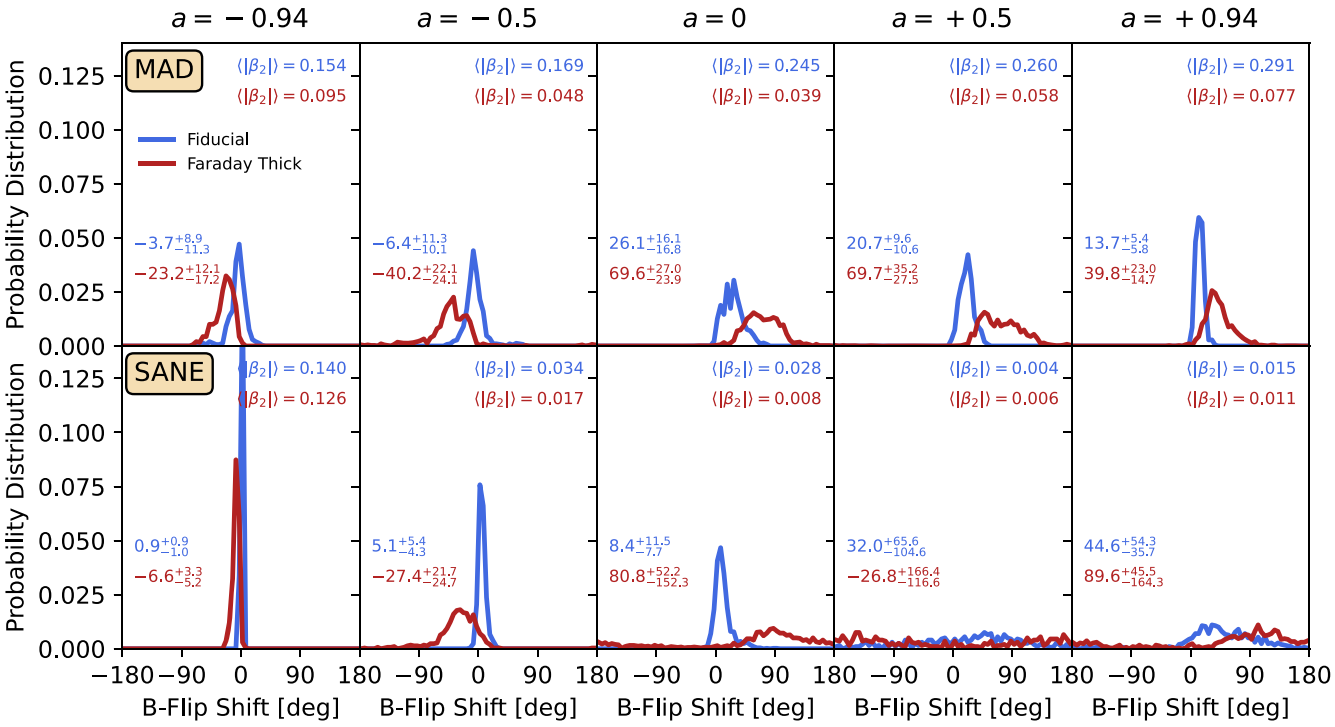

Figure 19. Differences in $\angle\beta_2$ between our anti-aligned and aligned magnetic field models ($\angle\beta_2(\mathrm{FR}_2) - \angle\beta_2(\mathrm{FR}_1)$). The effect of flipping the magnetic field is stronger for more Faraday Thick models, as expected. We find negative shifts in $\angle\beta_2$ for retrograde models and positive shifts for the others because these two sets of models are initialized with opposite magnetic field polarity by construction.

Appendix E
Distributions of $|\beta_2|$

Throughout this manuscript, we have focused on $\angle\beta_2$ rather than $|\beta_2|$. Our analytic ring model can make no meaningful prediction for $|\beta_2|$ because it does not include radial evolution nor does it account for Faraday rotation. We plot the distributions of $|\beta_2|$ for our Fiducial and Faraday Thick (aligned magnetic field) models in Figure 20. As discussed in previous works (Palumbo et al. 2020; Event Horizon Telescope Collaboration et al. 2021b), $|\beta_2|$ is larger for MAD models than for SANE models. In addition, as we had expected when making these model sets, our Faraday Thick models have lower $|\beta_2|$ than the Fiducial models. As discussed in Event Horizon Telescope Collaboration et al. (2021b), the $a = -0.94$ SANE models have uncharacteristically large $|\beta_2|$ because much of the polarization signal comes from the forward jet, which avoids the large Faraday rotation depth in the midplane.

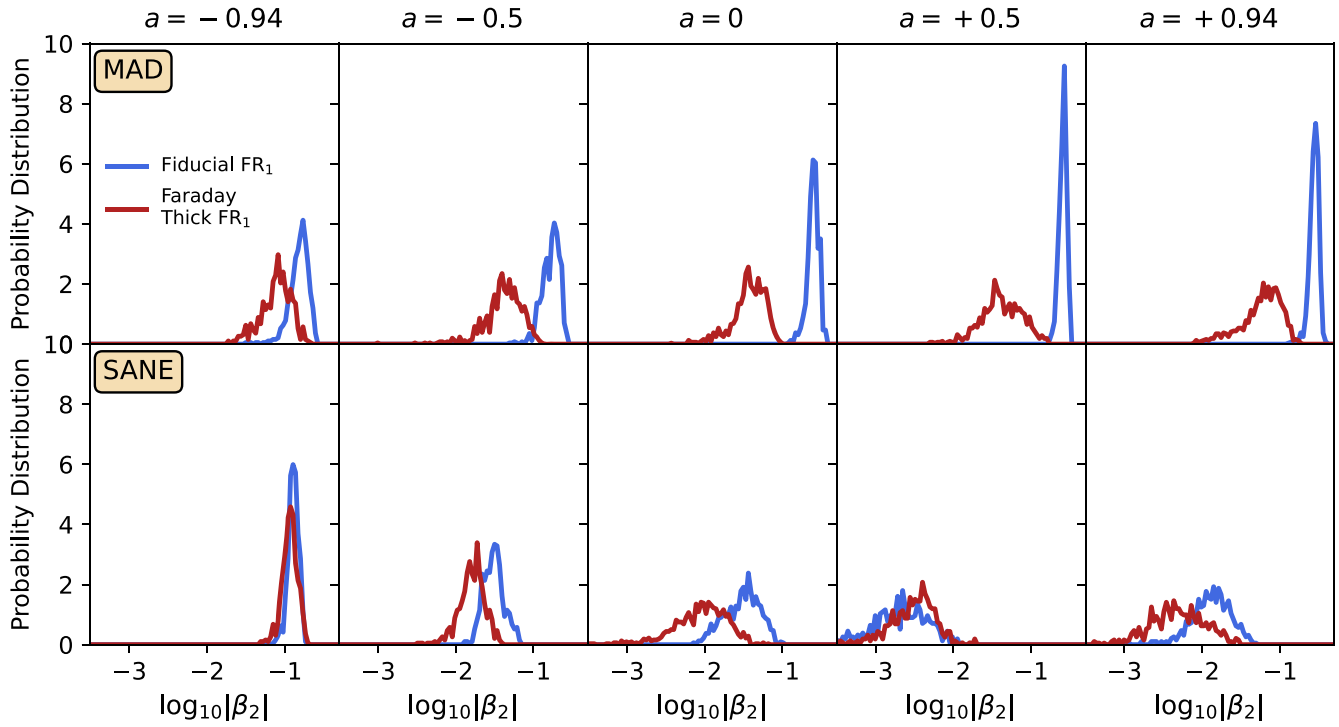

Figure 20. Distributions of $|\beta_2|$ for our models with aligned magnetic fields. Faraday rotation drives the most important trends: both SANE models and models with larger values of $R_{\rm high}$ and $R_{\rm low}$ have increased Faraday depths, which scrambles $|\beta_2|$.

ORCID iDs

Razieh Emami https://orcid.org/0000-0002-2791-5011
Angelo Ricarte https://orcid.org/0000-0001-5287-0452
George N. Wong https://orcid.org/0000-0001-6952-2147
Daniel Palumbo https://orcid.org/0000-0002-7179-3816
Dominic Chang https://orcid.org/0000-0001-9939-5257
Sheperd S. Doeleman https://orcid.org/0000-0002-9031-0904
Avery E. Broderick https://orcid.org/0000-0002-3351-760X
Ramesh Narayan https://orcid.org/0000-0002-1919-2730
Maciek Wielgus https://orcid.org/0000-0002-8635-4242
Lindy Blackburn https://orcid.org/0000-0002-9030-642X
Ben S. Prather https://orcid.org/0000-0002-0393-7734
Andrew A. Chael https://orcid.org/0000-0003-2966-6220
Richard Anantua https://orcid.org/0000-0003-3457-7660
Koushik Chatterjee https://orcid.org/0000-0002-2825-3590
Ivan Marti-Vidal https://orcid.org/0000-0003-3708-9611
Jose L. Gómez https://orcid.org/0000-0003-4190-7613
Kazunori Akiyama https://orcid.org/0000-0002-9475-4254
Matthew Liska https://orcid.org/0000-0003-4475-9345
Lars Hernquist https://orcid.org/0000-0001-6950-1629
Mark Vogelsberger https://orcid.org/0000-0001-8593-7692
Charles Alcock https://orcid.org/0000-0002-7892-3636
Randall Smith https://orcid.org/0000-0003-4284-4167
James Steiner https://orcid.org/0000-0002-5872-6061
Paul Tiede https://orcid.org/0000-0003-3826-5648
Freek Roelofs https://orcid.org/0000-0001-5461-3687

References

Anantua, R., Emami, R., Loeb, A., & Chael, A. 2020, ApJ, 896, 30
Balbus, S. A., & Hawley, J. F. 1991, ApJ, 376, 214
Bisnovatyi-Kogan, G. S., & Ruzmaikin, A. A. 1974, Ap&SS, 28, 45
Chael, A., Rowan, M., Narayan, R., Johnson, M., & Sironi, L. 2018, MNRAS, 478, 5209
de Buyl, P., Huang, M.-J., & Deprez, L. 2016, arXiv:1608.04904
De Villiers, J. -P., Hawley, J. F., & Krolik, J. H. 2003, ApJ, 599, 1238
Emami, R., Anantua, R., Chael, A. A., & Loeb, A. 2021, ApJ, 923, 272
Event Horizon Telescope Collaboration, Akiyama, K., Alberdi, A., et al. 2019b, ApJL, 875, L2
Event Horizon Telescope Collaboration, Akiyama, K., Alberdi, A., et al. 2019a, ApJL, 875, L1
Event Horizon Telescope Collaboration, Akiyama, K., Alberdi, A., et al. 2019c, ApJL, 875, L3
Event Horizon Telescope Collaboration, Akiyama, K., Alberdi, A., et al. 2019d, ApJL, 875, L4
Event Horizon Telescope Collaboration, Akiyama, K., Alberdi, A., et al. 2019e, ApJL, 875, L5
Event Horizon Telescope Collaboration, Akiyama, K., Alberdi, A., et al. 2019f, ApJL, 875, L6
Event Horizon Telescope Collaboration, Akiyama, K., Algaba, J. C., et al. 2021a, ApJL, 910, L12
Event Horizon Telescope Collaboration, Akiyama, K., Algaba, J. C., et al. 2021b, ApJL, 910, L13
Gammie, C. F., McKinney, J. C., & Toth, G. 2003, ApJ, 589, 444
Gelles, Z., Himwich, E., Johnson, M. D., & Palumbo, D. C. M. 2021, PhRvD, 104, 044060
Goddi, C., Marti-Vidal, I., Messias, H., et al. 2021, ApJL, 910, L14
Hunter, J. D. 2007, CSE, 9, 90
Igumenshchev, I. V., Narayan, R., & Abramowicz, M. A. 2003, ApJ, 592, 1042
Mizuno, Y., Fromm, C. M., Younsi, Z., et al. 2021, MNRAS, 506, 741
Moscibrodzka, M., Falcke, H., & Shiokawa, H. 2016, A&A, 586, A38
Mościbrodzka, M., & Gammie, C. F. 2018, MNRAS, 475, 43
Narayan, R., Igumenshchev, I. V., & Abramowicz, M. A. 2003, PASJ, 55, L69
Narayan, R., Palumbo, D. C. M., Johnson, M. D., et al. 2021, ApJ, 912, 35
Narayan, R., Sądowski, A., Penna, R. F., & Kulkarni, A. K. 2012, MNRAS, 426, 3241
Narayan, R., & Yi, I. 1995, ApJ, 444, 231
Oliphant, T. E. 2007, CSE, 9, 10
Palumbo, D. C. M., Wong, G. N., & Prather, B. S. 2020, ApJ, 894, 156
Prather, B., Wong, G., Dhruv, V., et al. 2021, JOSS, 6, 3336
Reback, J., jbrockmendel, McKinney, W., et al. 2021, pandas-dev/pandas: Pandas 1.3.2, v1.3.2, Zenodo, doi:10.5281/zenodo.5203279
Ricarte, A., Palumbo, D. C. M., Narayan, R., Roelofs, F., & Emami, R. 2022, ApJL, 941, L12
Ricarte, A., Qiu, R., & Narayan, R. 2021, MNRAS, 505, 523
Semenov, V., Dyadechkin, S., & Punsly, B. 2004, Sci, 305, 978
Shapiro, S. L., Lightman, A. P., & Eardley, D. M. 1976, ApJ, 204, 187
Tsunetoe, Y., Mineshige, S., Kawashima, T., et al. 2022a, ApJ, 931, 25
Tsunetoe, Y., Mineshige, S., Kawashima, T., et al. 2022b, Galax, 10, 103
van der Walt, S., Colbert, S. C., & Varoquaux, G. 2011, CSE, 13, 22
Waskom, M., Botvinnik, O., Ostblom, J., et al. 2020, mwaskom/seaborn: v0.10.0 (January 2020), Zenodo, doi:10.5281/zenodo.3629446
Wielgus, M., Akiyama, K., Blackburn, L., et al. 2020, ApJ, 901, 67
Wong, G. N., Prather, B. S., Dhruv, V., et al. 2022, ApJS, 259, 64